Petroleum Science 23 (2026) 742–761

Contents lists available at ScienceDirect

Petroleum Science

journal homepage: www.keaipublishing.com/en/journals/petroleum-science

Original Paper

Application of a CWFS model-based brittleness index for evaluating anisotropic brittleness in terrestrial shale under triaxial stress

Jun Zhang [a], Jin-Yuan Zhang [a], Jia Zeng [a,*], Zhe-Jun Pan [a], Yu-Wei Li [b,**], Zi-Yuan Cong [b]

[a] State Key Laboratory of Continental Shale Oil, Northeast Petroleum University, Daqing, 163318, Heilongjiang, China
[b] School of Environment, Liaoning University, Shenyang, 110036, Liaoning, China

ARTICLE INFO

Article history:
Received 22 June 2025
Received in revised form
25 November 2025
Accepted 25 November 2025
Available online 1 December 2025

Edited by Jia-Jia Fei

Keywords:
Shale
Brittleness index
Anisotropy
Friction strengthening
Cohesion weakening

ABSTRACT

For shale reservoir operations, assessing the brittleness of anisotropic shales is vital of optimizing wellbore stability analysis and fracturing design. Current brittleness indices lack effectiveness in characterizing shale brittleness anisotropy. Consequently, the experimental results reported in this paper derived from triaxial tests conducted on shale core samples from the Qingshankou Formation of the Songliao Basin. This study investigates the anisotropy of shale failure patterns and mechanical properties with respect to the bedding plane dip angle (θ), and quantifies the effect of confining pressure. Building on the cohesion weakening and friction strengthening (CWFS) theory, we established a novel triaxial brittleness index (B_t). This index uniquely combines the uniaxial brittleness index (B_u), reflecting inherent brittleness, with the brittleness weakening coefficient (B_w), quantifying the effect of confining pressure. Assessment of the anisotropic brittleness of shale based on B_t under varying confining pressures reveals that B_t first increases but then decreases with increasing θ. The brittleness peaks at $\theta = 0°$ and reaches its lowest point at $\theta = 60°$, a trend that aligns closely with the observed variations in the failure patterns of shale. Furthermore, the ability of the confining pressure to decrease shale brittleness varies with θ. At $\theta = 0°$, the uniaxial brittleness is the highest, but the confining pressure has the strongest weakening effect on shale brittleness. In contrast, the uniaxial brittleness at $\theta = 90°$ is second only to that at 0°, but the brittleness in this direction is least affected by the confining pressure. Compared with the five existing brittleness indices, the proposed index accounts for both inherent and apparent brittleness. It is more sensitive to internal lithological characteristics and external stress conditions and has strong potential for integration with geophysical data. This study provides valuable guidance for sweet spot identification, wellbore stability assessment, and fracturing scheme optimization in shale oil and gas exploration.

1. Introduction

Shale oil, recognized as a pivotal clean energy source, is gaining increased attention amidst the advancement of unconventional oil and gas resources. Its economical and efficient recovery necessitates the application of horizontal drilling coupled with multi-cluster hydraulic fracturing. Horizontal wells increase the contact length and oil discharge area between the wellbore and reservoir, while the fracture network generated by hydraulic fracturing enhances the permeability of shale formations (Zhang et al., 2022b; Zhang et al., 2023a, 2023b; Gu et al., 2024; Yan et al., 2025). Horizontal drilling and hydraulic fracturing critically depend on the precise determination of essential reservoir mechanical parameters, notably in-situ stress, strength, and Young's modulus. Generally, higher brittleness increases the risk of wellbore collapse during drilling, as documented by Holt et al. (2015) and Gui et al. (2018). Concurrently, it promotes the formation of intricate fracture networks under hydraulic stimulation, a phenomenon supported by Zhang et al. (2016). However, shale, being a sedimentary rock, demonstrates pronounced mechanical anisotropy owing to its intricate bedding structure and mineral composition. This

* Corresponding author.
** Corresponding author.
E-mail addresses: zengjia@nepu.edu.cn (J. Zeng), liyuweibox@126.com (Y.-W. Li).

Peer review under the responsibility of China University of Petroleum (Beijing).

https://doi.org/10.1016/j.petsci.2025.11.045

List of symbols

θ	inclination angle of bedding planes, °
σ_c	uniaxial compressive strength, MPa
σ_t	uniaxial tensile strength, MPa
σ_{tc}	the measured triaxial compressive strength, MPa
σ'_{tc}	the limiting triaxial compressive strength corresponding to the linear Mohr shear strength curve, MPa
C_0	cohesion under uniaxial stress, MPa
φ_0	internal friction angle under uniaxial stress, °
C_t	cohesion under triaxial stress, MPa
φ_t	internal friction angle under triaxial stress, °
q_f	frictional component during rock failure in the CWFS model
q_c	cohesive component during rock failure in the CWFS model
β	rupture angle of the shale sample, °
B_u	brittleness index without confining pressure
B_w	weakening coefficient reflecting the effect of confining pressure on rock brittleness
B_t	triaxial brittleness index

anisotropy affects the strength and deformation of shale, directly impacting its brittleness and influencing fracture propagation during hydraulic fracturing. Hence, research on the mechanical anisotropy of shale, specifically its anisotropic brittleness, is the key to improving hydraulic fracturing outcomes during shale oil extraction.

By comparing three different types of shale, Wu et al. (2020) and Patel et al. (2022) reported that shale rich in clay has stronger anisotropic characteristics. In addition to the influence of mineral composition, the bedding planes in the shale matrix, which act as weak planes, significantly affect its strength and fracture mode (Yang et al., 2020). In the past few decades, many researchers have conducted various laboratory tests to explore the anisotropic properties of various mechanical properties of shale. Uniaxial compression experiments by Wang and Li (2017) revealed that the dip angle of a bedding plane (θ) significantly affects the mechanical properties and velocity response of rocks, with longitudinal and transverse wave velocities decreasing with increasing bedding angle. Through a series of triaxial compressive strength tests, Jia et al. (2021) and Dong et al. (2024) reported that the failure modes of shale with different bedding angles (θ) can be divided into five types. In addition, the compressive strength tends to first decrease but then increase with increasing bedding angle. Heng et al. (2015) investigated the anisotropy of shale shear strength parameters and reported that the shear strength, cohesion, and internal friction angle reached their maximum and minimum values at $\sigma = 60°$ and $\sigma = 0°$, respectively. Ma et al. (2023) further reported that the fracture toughness and tensile strength of shale gradually increase with increasing bedding angle. However, according to Wang et al. (2023), Brazilian splitting samples frequently undergo significant shear displacement along bedding planes, while their tensile strength reaches a nadir at $\theta = 60°$. Kong et al. (2022) investigated the anisotropic characteristics of energy evolution in shale under cyclic loading, and the results revealed that elastic energy storage was greatest at 15°, and lowest at 60° and 90°. The dissipated energy in the 45° and 75° bedding directions is much greater than that in the other bedding directions. In addition to its macroscopic mechanical properties, shale exhibits significant anisotropy at the microscopic scale. Wu et al. (2020) reported through cross scale, big data based statistical nanoindentation techniques that shale exhibits multiscale elastic anisotropy. Through microindentation tests, Ma et al. (2024) reported that the microhardness, elastic modulus, compressive strength, and brittleness of shale in the normal parallel bedding direction are greater than those in the vertical bedding direction, whereas the fracture toughness shows the opposite pattern. Compared with the extensive research on the anisotropy of other mechanical parameters, relatively little has been conducted on shale brittleness anisotropy, with most studies focusing on the Longmaxi Formation shale in Sichuan, China (Geng et al., 2016). However, the shale brittleness anisotropy obtained is quite different. For example, Wang et al. (2017b) and Gui et al. (2023) reported that the trend of shale brittleness with increasing bedding angle is similar, however, Wang reported that shale brittleness reaches its maximum value at a bedding angle of 30° or 60°, whereas Gui reported that the shale brittleness index is the lowest at a bedding angle of 60°. Meanwhile, Zhang et al. (2017) reported that shale brittleness decreases first but then increases with increasing bedding angle, with the lowest brittleness occurring at 60°. The main reason is that there is currently no suitable method for evaluating the anisotropic brittleness of shale. At present, the brittleness indices for rock materials can be broadly categorized into five types. The first category relies on the proportion of brittle minerals within the rock composition (Jarvie et al., 2007; Wang and Gale, 2009; Glorioso and Rattia, 2012; Alzahabi et al., 2015). This approach stems from the understanding that minerals such as quartz and feldspar are key contributors to rock brittleness and fracture. However, these methods often fail to capture brittle anisotropy because they ignore the influence of rock diagenesis and stress conditions, i.e. mineral composition does not change with changes in bedding direction. The second category utilizes elastic properties determined through analysis of well log data (Rickman et al., 2008; Guo et al., 2015). This viewpoint posits that brittleness is positively correlated with material stiffness (elastic modulus), but inversely correlated with Poisson's ratio. Nevertheless, the variation in the Poisson's ratio with θ lacks a consistent trend, hindering the precise assessment of shale brittleness using such approaches. The third and fourth categories of brittleness indices are both derived from the mechanical parameters reflected in the stress–strain curve obtained through rock mechanics tests. The former approach assesses rock brittleness through deformation characteristics (Andreev, 1995; Hajiabdolmajid and Kaiser, 2003; Gong and Sun, 2015), whereas the latter directly links brittleness to the bearing capacity or strength parameters (Bishop, 1967; Altindag, 2003, 2010; Özfirat et al., 2016). Owing to the influence of bedding planes, shale stress–strain curves frequently display pronounced fluctuations both before and after peak stress. This behaviour complicates the identification of key characteristic points on the curve. For example, calculating brittleness indices that depend on the post-failure curve's strength decline rate and magnitude requires precise determination of residual strength. Brittleness indices of the fifth category utilize energy-based principles governing rock failure, specifically quantifying prepeak energy storage and post-failure dissipation dynamics (Tarasov and Randolph, 2011; Ai et al., 2016; Li et al., 2017). Brittleness indices derived from an energy perspective offer superior insight into rock failure, as they explicitly account for the energy dissipation governing brittle fracture, revealing its underlying mechanics more faithfully than traditional metrics. At present, energy-based brittleness indices have become relatively scientific methods for evaluating rock brittleness, but they also have two limitations when evaluating shale brittleness. On the one hand, the highly developed bedding planes in shale cause the fracturing process to involve friction and

opening along these weak surfaces. This leads to significant fluctuations in the stress-strain curve, especially in the postpeak stage, making the determination of fracture strain energy and residual strain energy extremely difficult. On the other hand, the inability to combine energy parameters with geophysical logging data means that such methods cannot continuously characterize the brittleness of formations at different depths and have limited applicability.

In this study, the anisotropy of failure patterns and key mechanical properties in the Qingshankou Formation shale (Songliao Basin) was investigated using triaxial compression experiments. Building on the cohesion weakening friction strengthening (CWFS) constitutive framework, we analysed how cohesion weakening and friction strengthening correlate with strain energy evolution and brittle fracture modes. Analysis demonstrated that the intrinsic parameters of the internal friction angle and cohesion fundamentally govern the extrinsic mechanical response and energy dissipation characteristics of rock. On the basis of these findings, novel brittleness indices for uniaxial and triaxial stress states were developed and subsequently applied to quantify the anisotropy in shale brittleness under these conditions.

2. Geological setting

Located in Northeastern China, Songliao Basin ranks among the world's richest land-phase hydrocarbon basins. Within its central Gulong Depression, large deep and semideep lake systems developed, leading to the deposition of two extensive sequences of fine-grained lacustrine sediment. These constitute the high-quality Qingshankou and Nenjiang Formation source rocks, which host substantial shale oil resources. Vertically, the enriched shale oil layers are distributed mainly in the lower parts of the Qing-1 and Qing-2 members of the Qingshankou Formation. According to the sedimentary gyre, lithological characteristics, mineral composition, TOC, etc., it is divided into 9 oil layers (Q_1–Q_9). The Qingshankou shale is mainly composed of matrix pore-shingle seams, and the pore types include organic matter pore seams, clay mineral intergranular pores and solution pores. The nanoscale pore-seam system controlled by horizontal shale greatly improves the physical properties of the reservoir, with pore widths ranging from 70 to 5000 nm, accounting for more than 75% of the total surface porosity. The horizontal permeability under overpressure conditions ranges from 0.011×10^{-3} to 1.620×10^{-3} μm^2, with an average of 0.580×10^{-3} μm^2, and the vertical permeability is less than 0.0001×10^{-3} μm^2, forming a highly porous seepage zone in the horizontal direction. The shale in the Qingshankou Formation accounts for over 95% and is interbedded with a small number of thin layers of dolomite, shell limestone, and siltstone, but the thickness of each layer is generally only a few centimetres. XRD analysis was conducted on 9 Qingshankou Formation shale samples (Fig. 1). The quartz content ranges from 30.8% to 35.6%, with an average of 33.5%, while the feldspar contet ranges between 9.7% and 24.7%, with an average of 18.4%. Calcite and dolomite are the primary carbonate minerals and are present at 3.1%–10.4% (average: 6.1%). The clay mineral content varies from 32.8% to 41.8%, with an average value of 37.4%. The remaining minerals collectively constitute less than 10%. The clay fraction is dominated by illite (50%–90%), an illite-montmorillonite mixed layer (20%–40%), and chlorite (10%–30%).

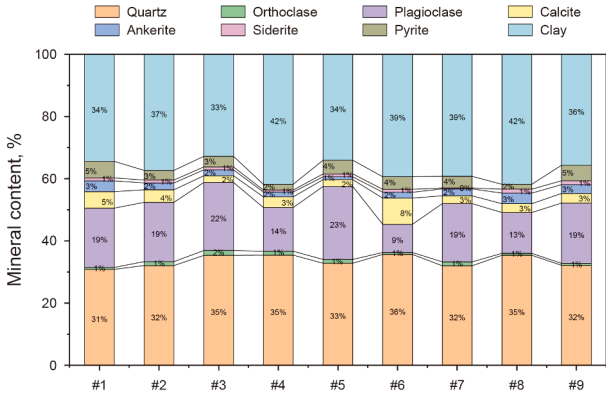

Fig. 1. Whole rock mineral content of the Qingshankou Formation shale.

3. Method for testing the anisotropic mechanical properties of shale

XRD analysis revealed that the Qingshankou shale contains a high proportion of brittle minerals (>50%), facilitating the formation of complex hydraulic fractures. However, the well-developed bedding system in the Qingshankou Formation induces significant anisotropy in the mechanical properties of the shale, altering the brittle failure characteristics in different directions and impacting hydraulic fracture propagation. To investigate the mechanical properties of the shale, particularly its brittle anisotropy, Brazilian splitting and conventional triaxial compression tests were conducted at the National Key Laboratory of Northeast Petroleum University, utilizing its GCTS RTR-1500 rock triaxial system (Fig. 2). Samples with seven distinct bedding plane orientations ($\theta = 0°$, 15°, 30°, 45°, 60°, 75°, and 90°; Fig. 3) were prepared and tested. To maintain the initial state of the sample as much as possible, the full-diameter sample was immediately wrapped and sealed with cling film until the preparation of the mechanical experiment sample begin. Owing to the high content of clay minerals in shale samples, their mechanical properties may deteriorate when exposed to water. In this experiment, shale samples were prepared into 25 × 50 mm and 50 × 25 mm sizes using wire-cutting equipment under anhydrous conditions. After online cutting, the samples were finely polished according to the ISRM (Ulusay, 2015) recommended method to ensure that the end face flatness error was less than 0.01 mm and that the diameter size error was less than 0.3 mm. Brazilian splitting tests were performed without confining pressure. Triaxial compression tests, however, applied confining pressures ranging from 0 to 30 MPa in 10 MPa increments (specifically, 0, 10, 20, and 30 MPa). All testing was implemented under axial displacement control. An initial preloading phase at 10 mm/min was applied until the axial load reached 1 kN. The displacement rate was subsequently switched to 0.06 mm/min for the main loading phase until sample failure. To reduce experimental variability and potential errors caused by instruments, shale samples with different bedding angles were

Fig. 2. GCTS RTR-1500 rock triaxial apparatus (high T&P capability).

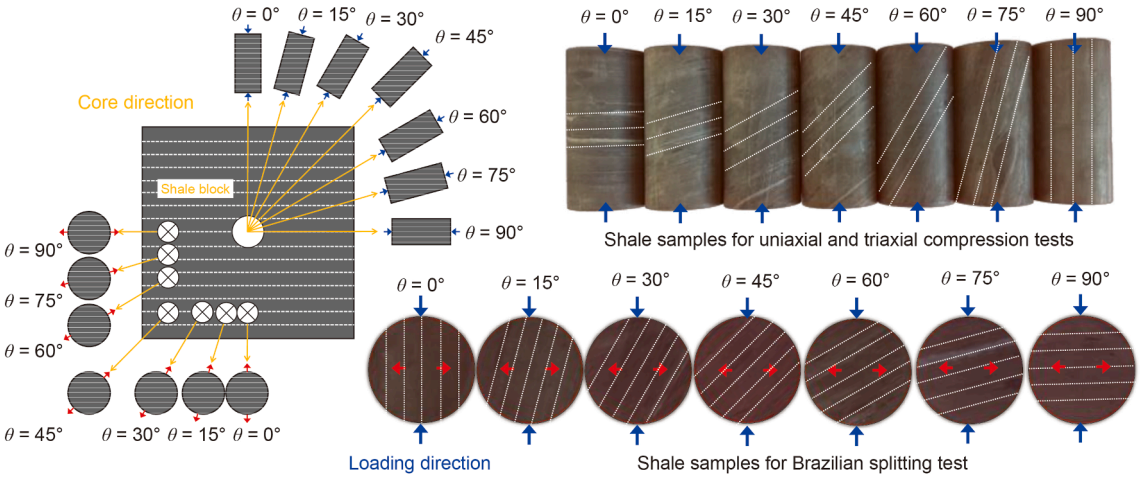

Fig. 3. Shale samples featuring varying bedding orientations subject to Brazilian splitting and triaxial compressive testing.

tested three times under various experimental conditions. Owing to space limitations, in this study, the sample with results closest to the average value was selected for typical analysis.

4. Anisotropy analysis of shale mechanical parameters

4.1. Failure patterns

For shale under triaxial compression, the final fracture patterns resulting from tests at varying confining pressures are shown in Fig. 4. Under uniaxial loading at $\theta = 0°$ and 15°, shale exhibits complex failure patterns, characterized by numerous longitudinal splitting cracks propagating parallel to the load axis and transecting the bedding planes. Additionally, the bedding planes along the crack path are activated, leading to shear slip. The simultaneous generation of multiple tensile splitting cracks and secondary shear cracks leads to significant radial expansion of the shale sample, a typical characteristic of high brittleness. Under a confining pressure of 10 MPa, constraints are imposed on both the initiation and development of matrix-hosted tensile cracks and the generation of shear cracks along the bedding planes. The failure pattern is characterized by a primary Y-shaped crack surrounded by several localized shear branches. As θ increases to 30°–45°, the tendency for matrix tensile failure in shale under uniaxial stress diminishes. Conversely, shear failure along the bedding planes becomes predominant, evolving into the primary failure mechanism. The samples commonly develop multiple subparallel bedding shear fractures, which connect via cross-layer tensile fractures within the matrix, ultimately resulting in a composite fracture system with a step-like morphology. Under confining pressure, the failure mechanism transitions towards shear-dominated failure penetrating across two bedding planes.

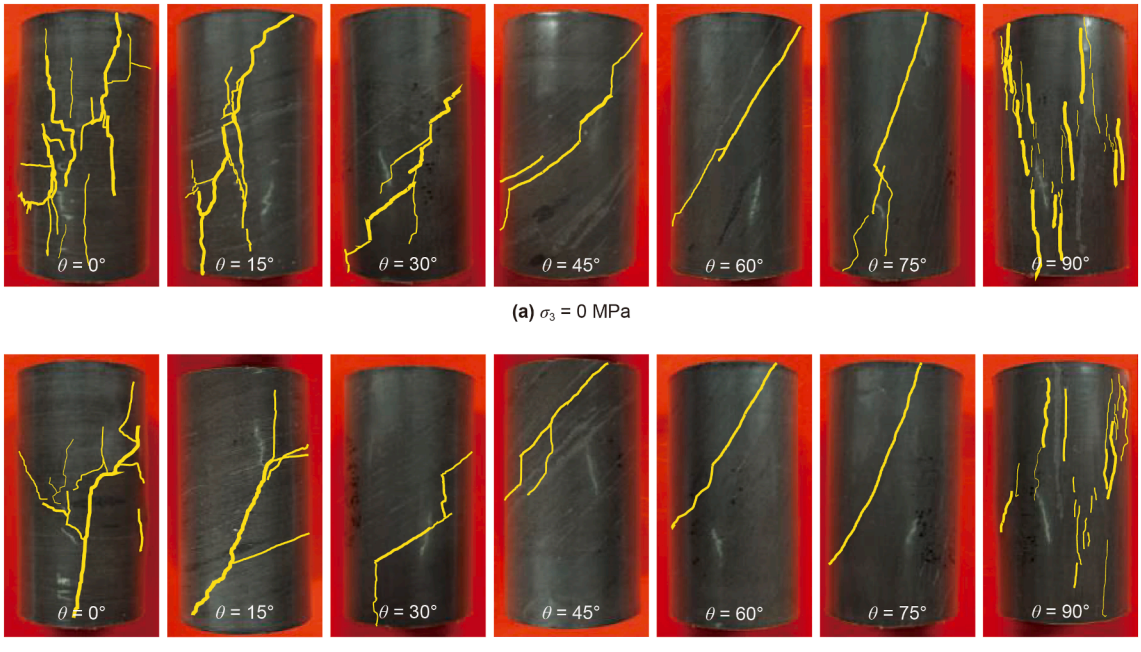

Fig. 4. (**a**) and (**b**) fracture characteristics of shale samples at varying inclination angles (θ) under confining pressures of 0 and 30 MPa, respectively.

When θ increases further to 60°–75°, both unconfined and confined conditions induce shale failure characterized by distinct shear cracks propagating subparallel to the bedding. At $\theta = 90°$, when the bedding aligns with the loading direction and is mechanically weaker than the matrix, multiple longitudinal tensile failures develop along the bedding planes, resulting in the formation of a longitudinal splitting failure pattern. Under a confining pressure of 10 MPa, the shale sample retains its dominant failure mode but shows reduced longitudinal tensile cracking along the bedding planes.

4.2. Stress-strain characteristics

The uniaxial stress-strain response of shale, as depicted in Fig. 5 for varying θ angles, reveals an initial distinct compaction stage. This characteristic is attributed to the material's high clay mineral content and well-developed bedding planes. Within the θ range of 0°–60°, failure occurs nearly linearly at the critical point, with shale samples demonstrating negligible plastic deformation before reaching peak stress. Additionally, the curves exhibit a rapid and sharp postpeak decline, which is a hallmark of brittle fracture. In contrast, the stress-strain curves of the shale samples inclined at $\theta = 75°$ and 90° display sawtooth patterns prior to peak stress. The correlation with the failure patterns in Fig. 4 suggests that these fluctuations near the peak arise from multiple longitudinal tensile splitting failures. A consistent trend is observed across Figs. 6–12: the stress-strain behaviour of the shale samples under varying confining pressures is similar for all θ values. Specifically, increasing the confining pressure enhances the prepeak plastic deformation, gradually increases the residual strength, and slows the postpeak stress decline. These trends suggest that shale brittleness decreases as the confining pressure increases.

4.3. Mechanical parameters

The variations in compressive strength with θ under different confining pressures in both Cartesian and polar coordinates are shown in Fig. 13. Under loading normal to the anisotropy axis ($\theta = 0°$), the normal stress on the bedding planes is maximized, resulting in shale failure characterized by tensile fracturing within the matrix (Fig. 4). Thus, shale sample at $\theta = 0°$ exhibit the highest uniaxial compressive strength. Over the range of θ from 0° to 30°,

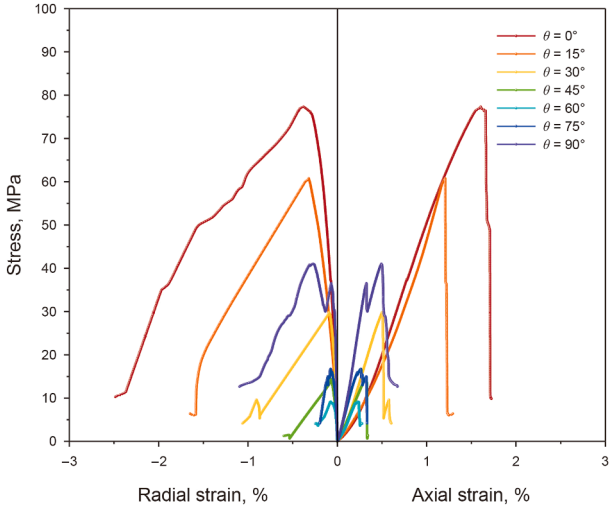

Fig. 5. Uniaxial stress-strain behaviour of shale at varying bedding plane orientations (θ).

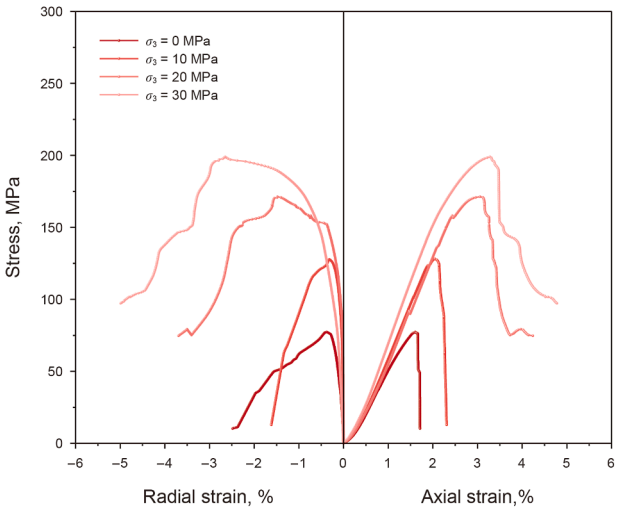

Fig. 6. Effects of confining pressure on shale stress-strain characteristics at $\theta = 0°$.

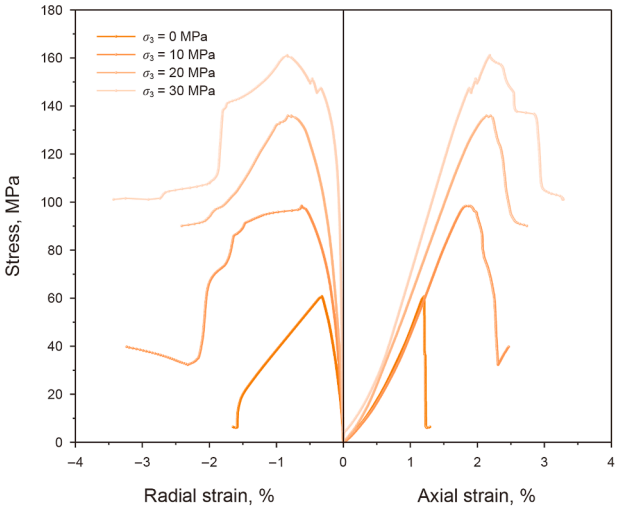

Fig. 7. Effects of confining pressure on shale stress-strain characteristics at $\theta = 15°$.

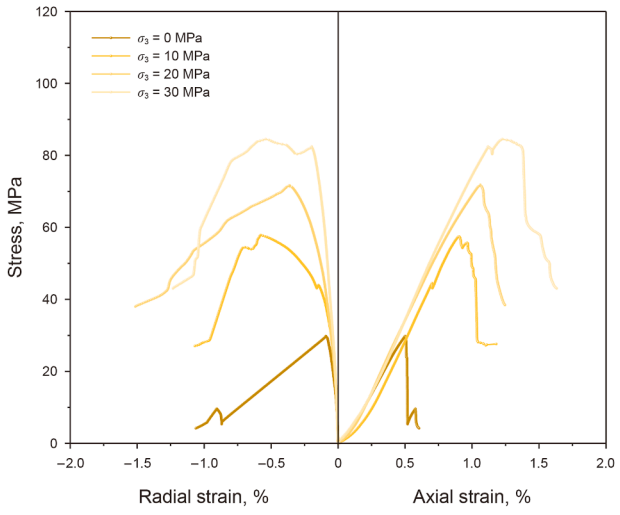

Fig. 8. Effects of confining pressure on shale stress-strain characteristics at $\theta = 30°$.

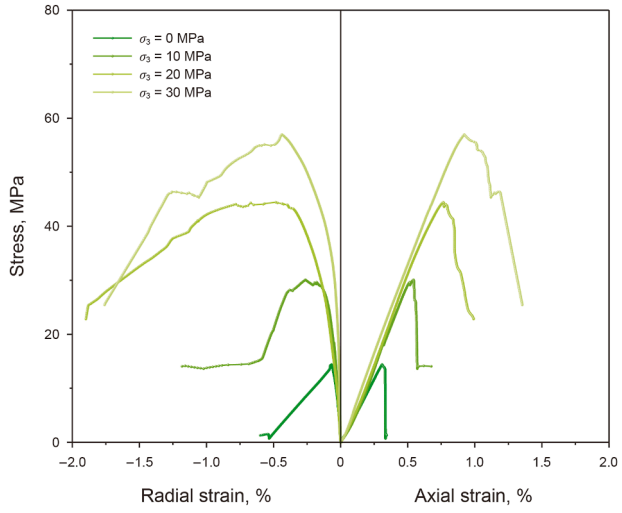

Fig. 9. Effects of confining pressure on shale stress-strain characteristics at $\theta = 45°$.

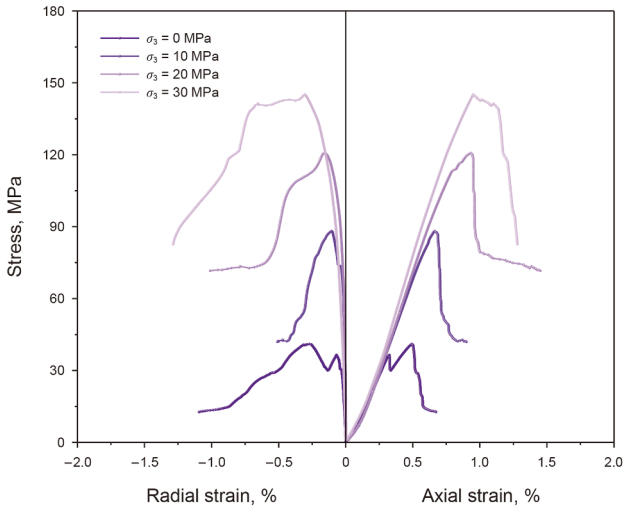

Fig. 12. Effects of confining pressure on shale stress-strain characteristics at $\theta = 90°$.

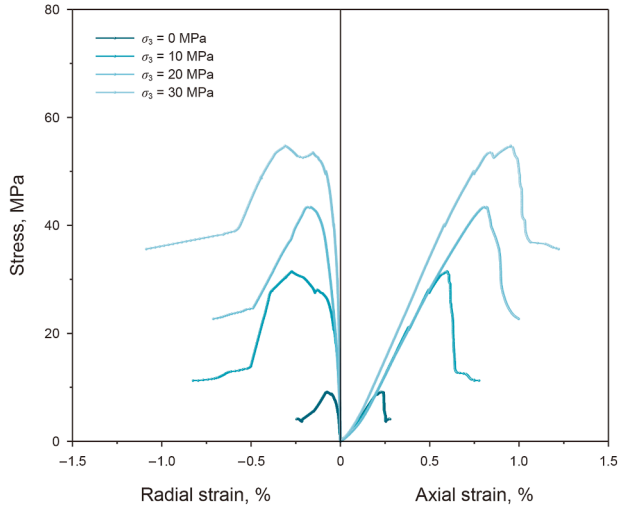

Fig. 10. Effects of confining pressure on shale stress-strain characteristics at $\theta = 60°$.

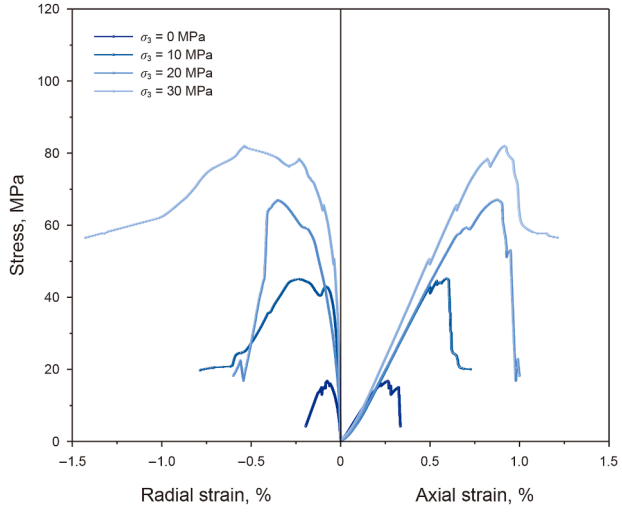

Fig. 11. Effects of confining pressure on shale stress-strain characteristics at $\theta = 75°$.

the normal stress acting on the bedding planes decreases gradually, while the shear stress concurrently increases. During this transition, shale failure is governed by both matrix tensile fracturing and shear slip along the bedding planes, gradually reducing the compressive strength. Within the θ range of 45°–60°, the bedding planes experience peak shear stress. Under axial loading, they loosen sufficiently to preclude achieving a fully compacted state. Consequently, shale samples primarily fail by shear along the bedding planes. Thus, the uniaxial compressive strength of the shale reaches its minimum at $\theta = 60°$. When θ exceeds 60°, the uniaxial compressive strength increases again. This shift occurs as the bedding orientation becomes more parallel with the loading axis, causing the dominant failure mechanism along the bedding planes to transition from shear to tensile splitting. However, constraints imposed by the loading platens suppress tensile crack development, ultimately leading to an increase in peak strength. Furthermore, the effect of confining pressure on shale strength manifests in two distinct ways across the range of bedding angles (θ). First, confining pressure increases the strength for all orientations, but the magnitude of this strengthening varies markedly: it is most substantial for orientations parallel and perpendicular to loading ($\theta = 0°$ and 90°), whereas it is minimal for intermediate angles ($\theta = 45°$ and 60°). Second, increasing the confining pressure does not alter the fundamental trend relating the peak strength to θ. The variations in the elastic modulus and Poisson's ratio with θ under different confining pressures are depicted in Figs. 14 and 15, respectively. Across all confining pressures, the elastic modulus increases modestly as θ increases from 0° to 45°, followed by a more substantial increase above 45°. Poisson's ratio clearly increases with confining pressure but shows only a weak dependence on θ.

Figs. 16 and 17 illustrate the anisotropic behaviour of cohesion and the internal friction angle across varying confining pressures. Under unconfined conditions ($\sigma_3 = 0$ MPa), both parameters exhibit pronounced anisotropy, decreasing initially before increasing with increasing bedding plane inclination θ. Notably, cohesion peaks at $\theta = 90°$, whereas the internal friction angle reaches its maximum at $\theta = 0°$. Furthermore, the magnitudes of both the cohesion and internal friction angle are dependent on the confining pressure: the cohesion is positively correlated with increasing σ_3, whereas the internal friction angle is negatively correlated.

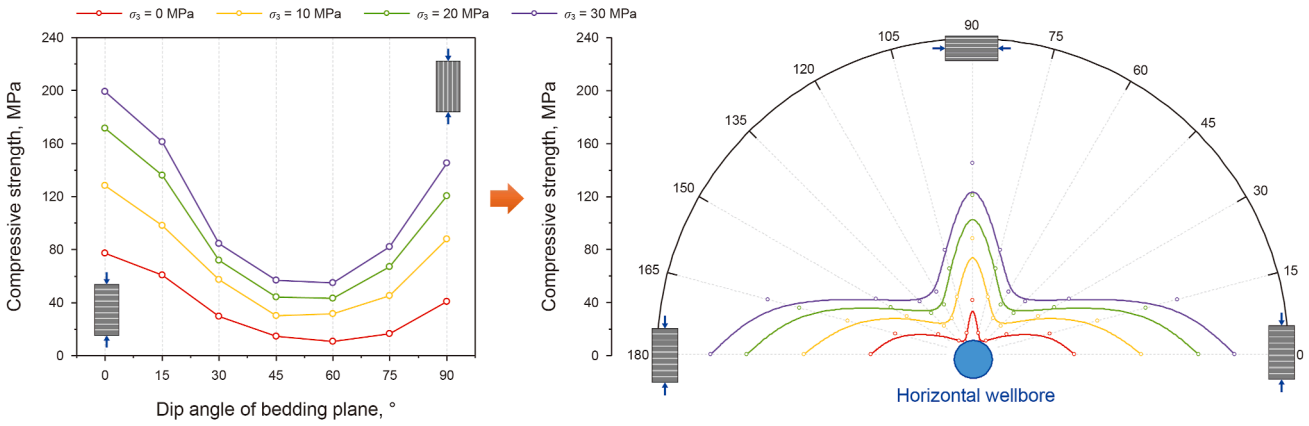

Fig. 13. Compressive strength vs. θ for different confining pressures, plotted in dual coordinate systems (Cartesian and polar).

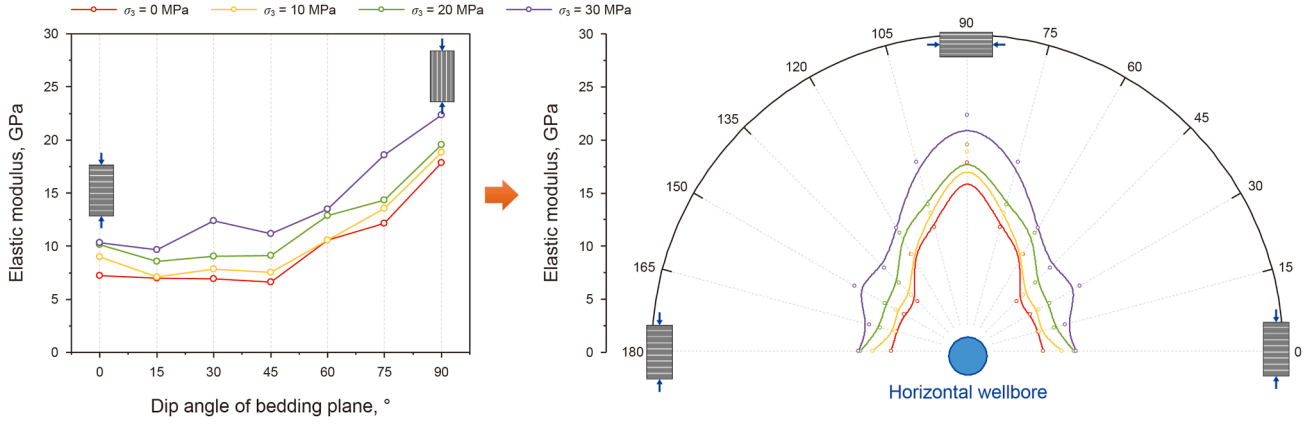

Fig. 14. Elastic modulus vs. θ for different confining pressures, plotted in dual coordinate systems (Cartesian and polar).

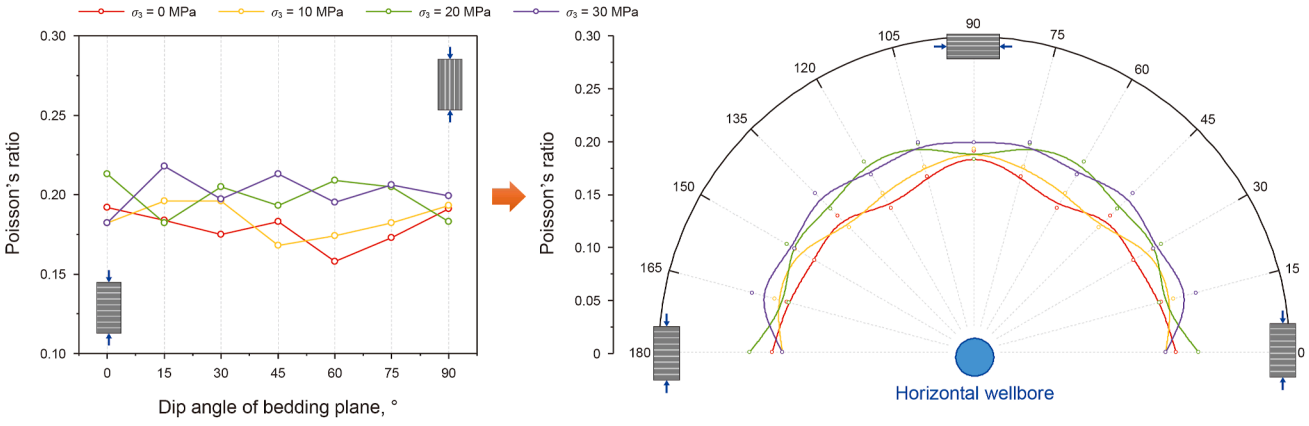

Fig. 15. Poisson's ratio vs. θ for different confining pressures, plotted in dual coordinate systems (Cartesian and polar).

5. Brittleness index based on the CWFS model

5.1. CWFS model and its correlation with rock brittleness

Hajiabdolmajid and Kaiser (2003) first proposed the CWFS model (Fig. 18(a)), suggesting that rock deformation to failure involves cohesion weakening and friction strengthening. During elastic deformation, cohesive forces between rock minerals resist external loads, with minimal shear sliding between particles. At this stage, rock strength primarily depends on the cohesive component. As the load increases and the internal tensile stress exceeds the cohesive strength, mineral particles rupture along the grain boundaries, resulting in the formation of tensile cracks. Subsequently, friction influences crack development, which increases as microcracks expand and accumulate. When the stress exceeds the peak strength, microcracks interconnect, forming macroscopic fractures, while cohesive and frictional forces stabilize with shear failure. Consequently, the progression of rock

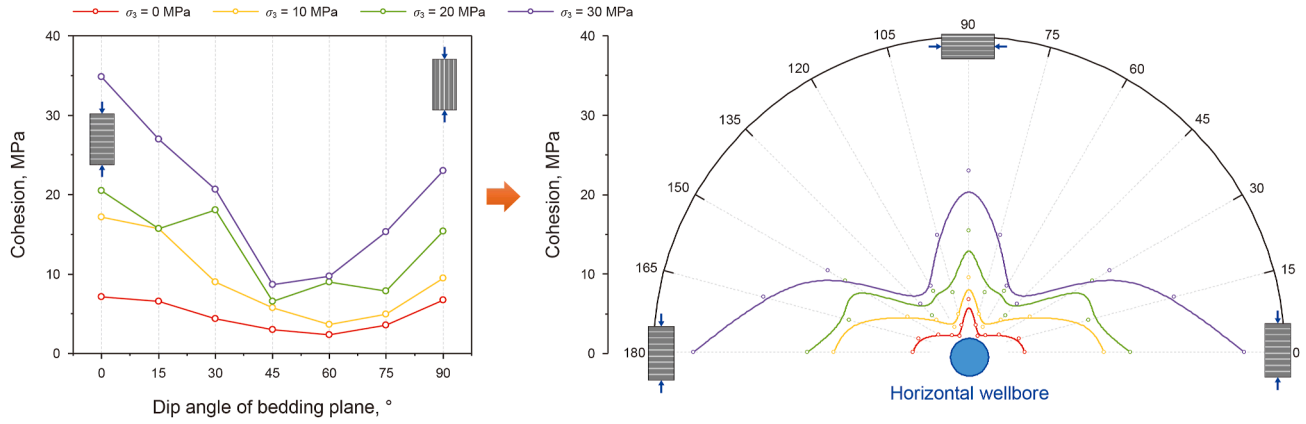

Fig. 16. Comparison of Cartesian and polar coordinate representations of cohesion variation with θ under multiple confining pressures.

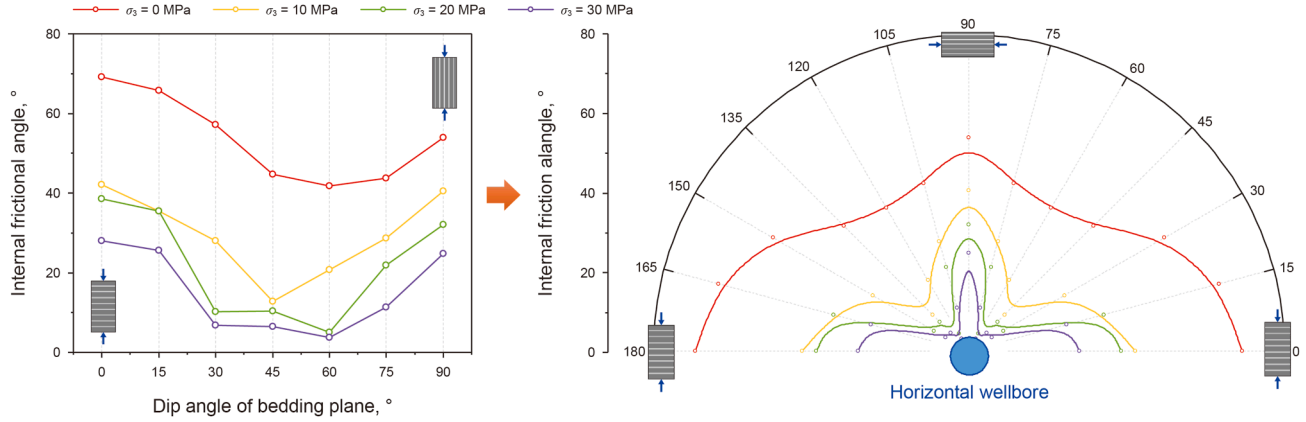

Fig. 17. Comparison of Cartesian and polar coordinate representations of internal frictional angle variation with θ under multiple confining pressures.

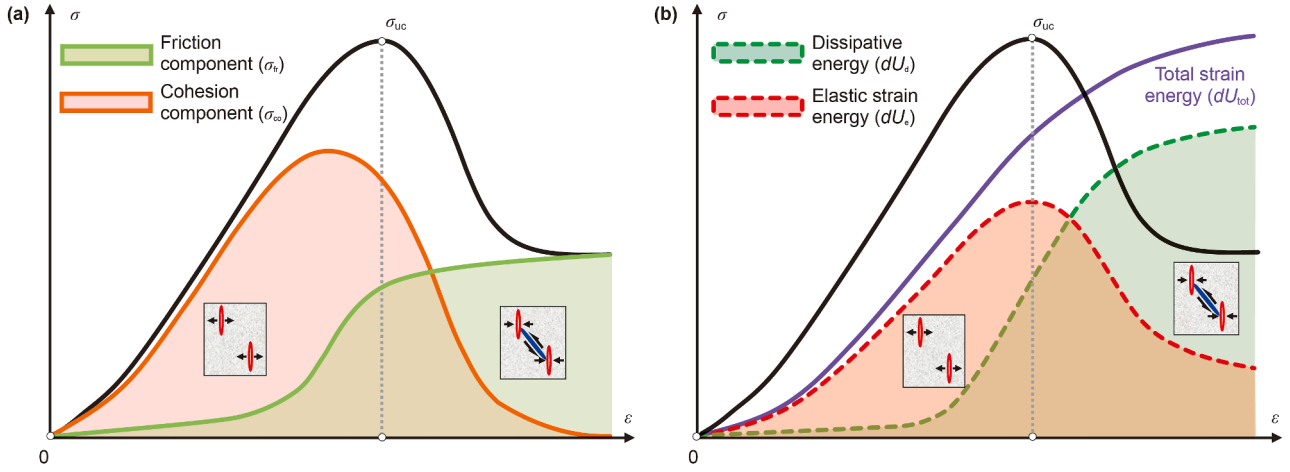

Fig. 18. (**a**) Evolving cohesive and frictional components within the CWFS model throughout the failure process. (**b**) Corresponding transformation in elastic versus dissipated energy within the energy model as failure advances.

deformation, damage, and ultimate failure stems from the interplay of cohesion and friction. Fundamentally, the internal friction angle and cohesion serve as the key mechanisms governing the transition to either brittle failure or plastic deformation in rock masses. Ramsay (1967) and Allaby and Allaby (1990) characterized brittleness as the ability of rock to convert its cohesion into inherent friction upon failure.

The energy dynamics governing rock failure are fundamentally linked to the activation of its cohesive and frictional resistance mechanisms. Fig. 18(b) demonstrates that the input work is

predominantly divided into stored elastic strain energy and dissipated energy. Elastic strain energy reflects the rock's capacity for energy storage and subsequent release, whereas dissipated energy fuels microcrack development prior to peak stress and drives macroscopic fracture propagation postpeak. Established indices quantifying brittleness through strain energy consistently show that rocks exhibiting higher brittleness store a larger proportion of the total input energy elastically, correspondingly reducing the fraction dissipated (Ai et al., 2016; Zhang et al., 2022; Jiang et al., 2023; Cheng et al., 2024). A comparison of the cohesion weakening friction strengthening (CWFS) model with strain energy evolution (Fig. 18) reveals a direct correspondence: cohesive strength mobilization governs elastic energy storage, while frictional resistance governs dissipation. Consequently, enhanced rock brittleness is correlated with diminished mobilization of the frictional component and reduced energy dissipation throughout deformation and failure. To investigate the impact of cohesive and frictional activation on brittle rock failure modes, the Mohr-Coulomb (M-C) failure criterion is integrated with the CWFS model framework, as shown in Fig. 19. The M-C failure surface, formulated in principal stresses (Eq. (2)), depends on parameters C_0 and φ_0 derived from uniaxial compressive strength (σ_c) and tensile strength (σ_t) tests (Eq. (1)).

$$\tau = \sigma \cdot \tan\varphi_0 + C_0 \tag{1}$$

$$f = (\sigma_1 - \sigma_3) - 2C_0 \cdot \cos\varphi_0 - (\sigma_1 + \sigma_3)\sin\varphi_0 \tag{2}$$

Therefore, the M-C criterion is also represented in the p-q coordinate system:

$$q = p \cdot \tan\alpha + a \tag{3}$$

where the mean stress $p = (\sigma_1 + \sigma_3)$, the deviatoric stress $q = (\sigma_1 - \sigma_3)$, and σ_1 and σ_3 denote the maximum and minimum principal

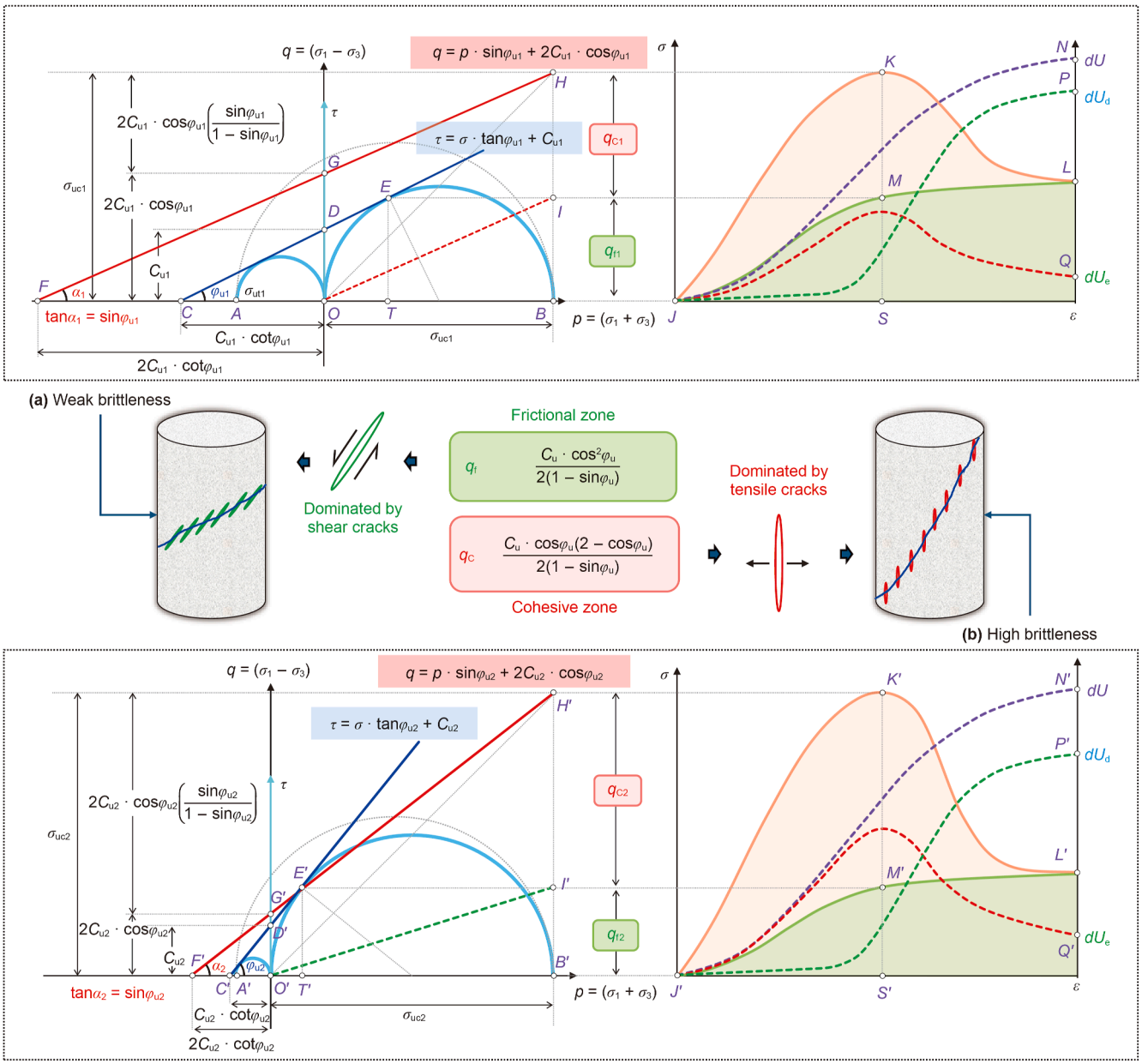

Fig. 19. (**a**) and (**b**) are the evolution of the cohesive and frictional components corresponding to rocks with weak and strong brittle fracture characteristics, respectively.

stresses, respectively. The relationships $\tan\alpha = \sin\varphi_0$ and $a = 2C_0\cos\varphi_0$ hold. Fig. 17 superimposes Eq. (1) and Eq. (3) within a shared plot. The blue curve depicts the material shear strength envelope within the σ-τ plane, whereas the red curve illustrates its counterpart within the p-q plane. Within this p-q plot, segment HB equals the uniaxial compressive strength σ_c (represented by OB). Consequently, the length HB (or KS) corresponds directly to the peak stress σ_c observed in the stress-strain response of the CWFS model. In the σ-τ representation, point E signifies the tangency between the Mohr-Coulomb failure envelope and the Mohr circle for uniaxial compression. Thus, the distance ET quantifies the shear strength q_f at failure. Linking the CWFS model with the Mohr-Coulomb criterion reveals that $MS = ET = q_f$. This parameter q_f captures the shear stress component governing rock failure within the CWFS framework, specifically representing the mobilized frictional resistance upon damage initiation.

$$q_f = \frac{C_0{}^2\cos\varphi_0}{1-\sin\varphi_0} \tag{4}$$

KM in Fig. 19 represents the mobilized cohesive force component q_c, which can be expressed as follows:

$$q_c = \sigma_c - q_f = \frac{2C_0\cos\varphi_0}{1-\sin\varphi_0} - \frac{C_0{}^2\cos\varphi_0}{1-\sin\varphi_0} = \frac{C_0\cos\varphi_0(2-\cos\varphi_0)}{1-\sin\varphi_0} \tag{5}$$

From the perspective of microcrack evolution, cohesion mobilization stems from tensile failure at mineral particle intergranular interfaces, whereas friction mobilization arises from shear sliding. The continuous development and competition of these two types of microcracks determine the micromechanical mechanism of brittle fracture in rocks. As shown in Fig. 19, when cohesive mobilization is dominant, rock damage is characterized mainly by longitudinal tensile microcrack evolution, and eventually these tensile microcracks continue to connect to form macroscopic fractures. At this time, the rupture angle of the rock is $\beta_2 = \pi/4 + \varphi_{02}/2$. When frictional mobilization is dominant, the rock undergoes mainly shear microcrack evolution during the failure process, and the resulting macroscopic rupture angle is $\beta_1 = \pi/4 + \varphi_{01}/2$. In Fig. 19, $\varphi_{02} > \varphi_{01}$, which reflects that when crack evolution is dominated by the cohesive zone, rocks are more likely to form longitudinal splitting failure patterns with larger shear angles. As demonstrated by Wang et al. (2017a) and Kuang et al. (2021), brittle failure under low confining pressure constraints is typically characterized by a fracture mode dominated by tensile microcracks.

Both the uniaxial compressive strength and cohesive strength substantially increase as the internal friction angle increases (Fig. 20). In contrast, the frictional component exhibits minimal change. An elevated internal friction angle enhances shear stability between mineral particles and impedes the propagation of the shear microcracks. Consequently, the strain energy accumulated within the rock primarily drives the evolution of tensile microcracks, thereby intensifying the weakening effect on cohesion. Furthermore, the brittleness index ($(\sigma_c - q_f)q_f$), derived from the stress-strain curve, progressively increases with increasing internal friction angle. This trend is indicative of increasing rock brittleness (Liang et al., 2017; Xia et al., 2017). It can therefore be concluded that rock brittleness is significantly positively correlated with the internal friction angle, a conclusion that has already been confirmed in earlier studies (Hucka and Das, 1974). As shown in Fig. 21, cohesion is strongly positively correlated with the uniaxial compressive strength, as well as with both its cohesive and frictional components. This suggests that higher cohesion not only increases the overall rock strength but also enhances the contribution of both strength components. However, the strength drop coefficient remains constant with increasing cohesion, suggesting that the promotion of the cohesive component and the frictional component by cohesion occurs in a certain proportion, reflecting that cohesion does not affect the rock's brittleness.

5.2. Establishment of the brittleness index under uniaxial stress

(a) Step 1: Form of the Mohr-Coulomb criterion under the influence of confining pressure

Under ideal conditions, the ultimate shear strength curve is linear. However, in reality, the molar envelope of most rock materials is an arc-shaped curve with a gradually decreasing slope. To more accurately reflect the confining pressure effect of rocks, this paper derives the molar strength envelope equation in the form of a parabolic function:

$$\tau^2 = [(\sigma_c + 2\sigma_t) - 2\sqrt{\sigma_t(\sigma_c + \sigma_t)}](\sigma + \sigma_t) \tag{6}$$

The shear strength curve tangent to the envelope can be expressed as follows:

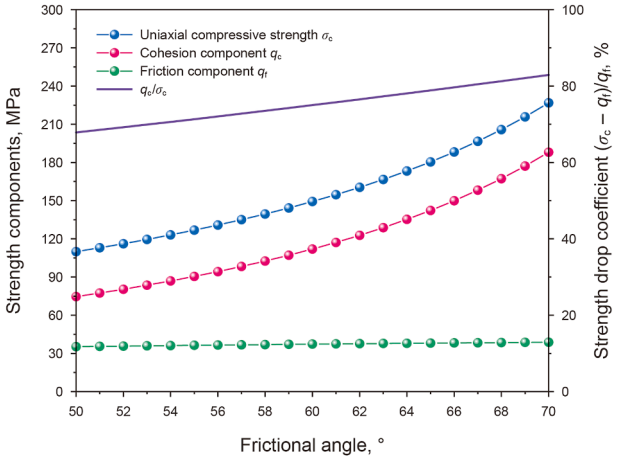

Fig. 20. Variation of various strength components with the internal friction angle.

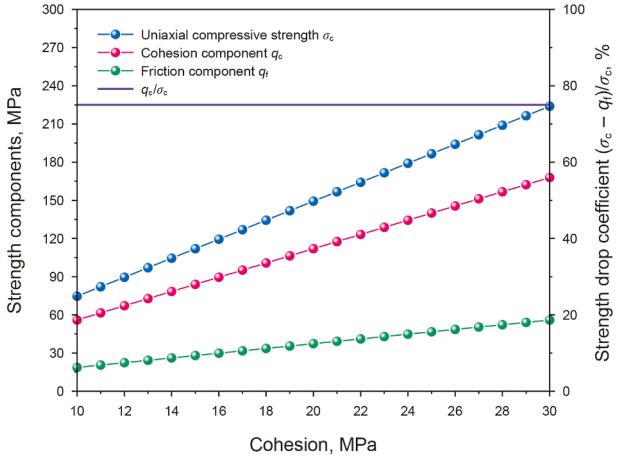

Fig. 21. Variation of various strength components with cohesion.

$$\tau=\sigma\frac{\sqrt{\sigma_t\sigma_c+2(\sigma_t)^2-2\sigma_t\sqrt{\sigma_t(\sigma_t+\sigma_c)}}}{2\sigma_t}+\sqrt{\sigma_t\sigma_c+2(\sigma_t)^2-2\sigma_t\sqrt{\sigma_t(\sigma_t+\sigma_c)}} \tag{7}$$

In this form, the uniaxial compressive strength (σ_c) and uniaxial tensile strength (σ_t) can be expressed as

$$\begin{cases}\sigma_t=\dfrac{C_0}{2\tan\varphi_0}\\ \sigma_c=2C_0(\tan\varphi_0+1)\end{cases} \tag{8}$$

(b) Step 2: Principle and key parameters for constructing the uniaxial brittleness index

The Mohr stress circle features representing ideal plastic (a), elastic-plastic rock (b), and ideal brittle (c), materials are plotted in Fig. 22. Limit analysis is employed to define a brittleness index based on the internal friction angle. An auxiliary Mohr circle is defined by circumscribing the Mohr circles for the uniaxial tensile strength and compressive strength. Its centre is denoted as point Q. For an ideal plastic material, the tensile and compressive strengths are nearly equal, causing point Q in Fig. 22(a) to approach the origin (point O). However, as the internal friction angle increases, the disparity between uniaxial compressive strength and tensile strength increases progressively. Consequently, point Q shifts rightward along the normal stress (σ) axis, as depicted in Fig. 22(b). When the internal friction angle approaches 90°, the Mohr circle characteristic of an ideal brittle material is reflected, with point Q nearly coinciding with the centre G of the Mohr stress circle corresponding to the uniaxial compressive strength, as shown in Fig. 22(c). Therefore, it can be concluded that the distance ΔR between point Q and point G is a key parameter affecting the evolution of rock brittleness.

(c) Step 3: Determination of the characterization range of the uniaxial brittleness index

On the basis of the above rules, we can infer that under the nonlinear Mohr-Coulomb criterion, the brittleness of generalized materials can be measured by the ratio of the abscissa x_Q of the circumcircle centre to the abscissa x_G of the Mohr circle centre corresponding to uniaxial compression. Therefore, the brittleness index of generalized materials under uniaxial stress can be expressed as follows:

$$B_u=\frac{x_Q}{x_G} \tag{9}$$

However, existing research has shown that the compressive tensile strength ratio of rock materials is between 5 and 50 (Sari, 2018); thus, it is impossible for point Q to coincide with the origin or point G, that is, x_Q has a minimum and maximum value within (0, x_G). Therefore, the brittleness index applicable to rock materials can be expressed as follows:

$$B_u=\frac{x_Q-x_{Q\min}}{x_{Q\max}-x_{Q\min}}=\frac{10}{9}-\frac{25\cos^2\varphi_u}{18\sin\varphi_u(\sin\varphi_u+\cos\varphi_u)} \tag{10}$$

5.3. Establishment of the brittleness index under triaxial stress

(a) Step 1: Principle and key parameters for constructing the triaxial brittleness index

For hydrocarbon reservoir engineering applications where in-situ stress governs rock brittleness and fracture behaviour, advancing a confining-pressure-dependent triaxial brittleness index is essential. In Fig. 23, the red straight line represents the limit shear strength curve for ideal brittle materials, which is approximately linear. This suggests that cohesion, internal friction angle,

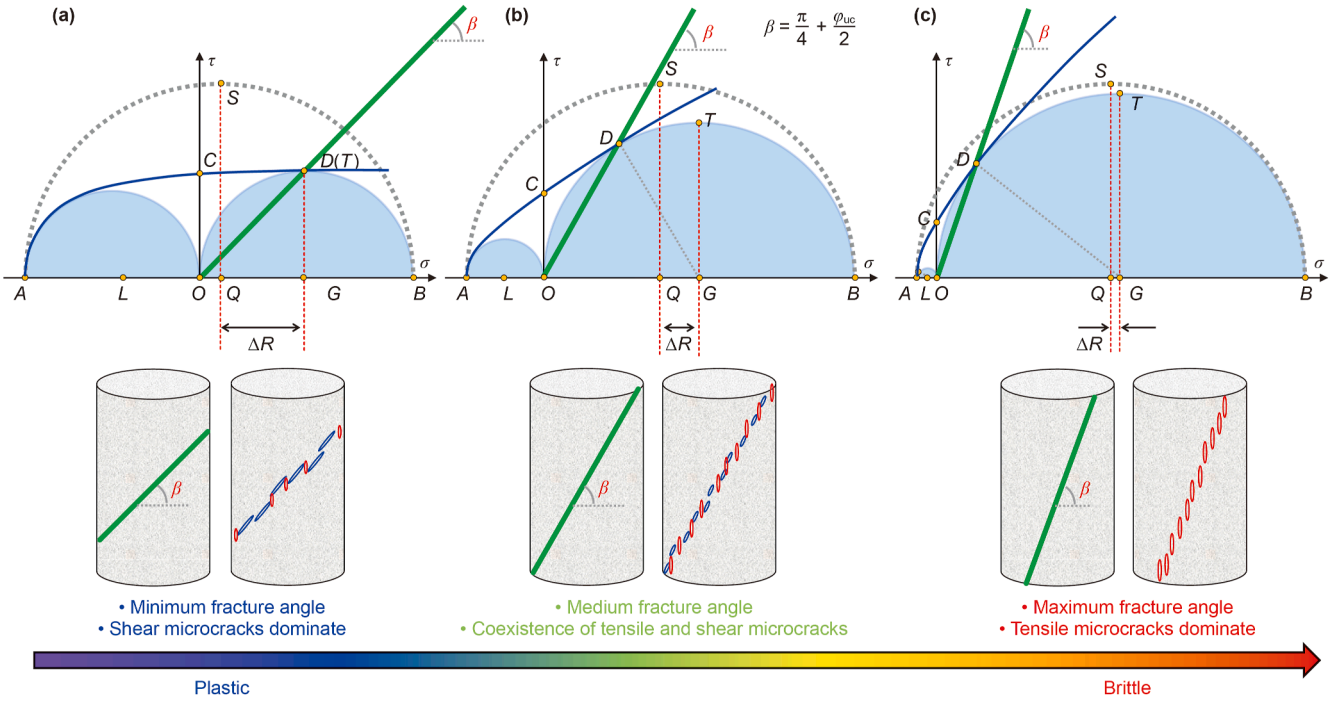

Fig. 22. Cohesive and frictional characteristics of different brittle rocks and their correlation with rock failure patterns.

and rupture angle remain constant under confining pressure, indicating that confining pressure does not affect rock brittleness. However, in reality, the Mohr stress circle characteristics of rock materials with brittle-plastic features under different stresses do not follow this pattern. As illustrated by the blue curve in Fig. 23, higher confining pressure causes the mineral particles within the rock to compact more tightly, enhancing cohesion but decreasing the shear stability of the rock. Concurrently, the internal friction angle gradually decreases, resulting in a Mohr shear strength curve that assumes a convex shape with progressively diminishing slopes (Byerlee, 1968; Barton, 1976). This is also why, in many studies (Akdag et al., 2021; Xia et al., 2022; Liu et al., 2024), the rock rupture angle tends to gradually decrease with increasing confining pressure. The primary mechanism underlying the confining pressure-induced decrease in rock brittleness involves its contrasting effects on strength parameters: the cohesion contribution is heightened, whereas the friction angle contribution is lessened, leading to changes in the rupture angle. This pattern is evident in the shale cohesion and internal friction angle data (Figs. 16 and 17). This core relationship provides a basis for defining a confining pressure sensitivity coefficient for brittleness.

(b) Step 2: Establishment of the brittleness weakening coefficient

Fig. 23 defines σ_{tc} (measured triaxial strength) and σ'_{tc} (theoretical linear Mohr-Coulomb limit strength) for a specific confining pressure. The underlying mechanism involves a progressive shift of the Mohr circle centre towards the coordinate origin as confining pressure increases. Therefore, the ratio of the measured strength to the theoretical limit strength, σ_{tc}/σ'_{tc}, constitutes an appropriate weakening coefficient (B_w) to represent the influence of confining pressure on brittleness.

$$B_w = \frac{\sigma_{tc}}{\sigma'_{tc}} = \frac{\sigma_{tc}}{\frac{2C_0\cos\varphi_0}{(1-\sin\varphi_0)} + \sigma_3\frac{(1+\sin\varphi_0)}{(1-\sin\varphi_0)}} \tag{11}$$

(c) Step 3: Establishment of the triaxial brittleness index

B_u represents the brittleness index of rock materials under nonconfining pressure conditions, while B_w represents the degree to which rock brittleness deteriorates because of confining pressure. Therefore, the product of these two can represent the brittleness under confining pressure conditions, which is defined as the triaxial brittleness index B_t in this paper.

$$B_t = B_u \cdot B_w \tag{12}$$

(d) Step 4: Extended form of the triaxial brittleness index B_t

Shen et al. (2018) revised the M-C criterion on the basis of previous experimental data and obtained a prediction formula (Eq. (12)) for the triaxial cohesion C_t and triaxial internal friction angle φ_t.

$$\begin{cases} C_t = C_0 + (\sigma_c - AC_0)\dfrac{\sigma_3}{2\sigma_c} \\ \varphi_t = \varphi_0\left(1 - B\sqrt{\dfrac{\sigma_3}{2\sigma_c}}\right) \end{cases} \tag{13}$$

Coefficients A and B are parameters determined by fitting data from multiple triaxial compression tests. The more widely applicable B_t can be expressed as follows:

$$B_t = B_u \cdot B_w = B_u \cdot \frac{C_t\cos\varphi_t + \sigma_3(1+\sin\varphi_t)}{C_0\cos\varphi_0 + \sigma_3(1+\sin\varphi_0)} \cdot \frac{(1-\sin\varphi_0)}{(1-\sin\varphi_t)} \tag{14}$$

5.4. Sensitivity analysis of the new brittleness indices

A presents a sensitivity analysis of the uniaxial brittleness index (B_u), confining pressure weakening coefficient (B_w), and the triaxial brittleness index (B_t) relative to the uniaxial internal friction angle and cohesion is shown in Fig. 24. B_u increases markedly with increasing friction angle, indicating that increased friction substantially enhances the inherent rock brittleness under uniaxial stress. Conversely, B_w decreases as the friction angle increases. B_t, however, exhibits a nonmonotonic relationship with the friction angle, first increasing to a maximum before declining gradually. This phenomenon occurs because excessive confining pressure amplifies the relative frictional resistance of shear cracks, thereby hindering the development of brittle fractures. Under low confining pressures, both tensile and shear microcracks evolve simultaneously. An increase in the internal friction angle promotes brittle fracture because frictional resistance suppresses shear

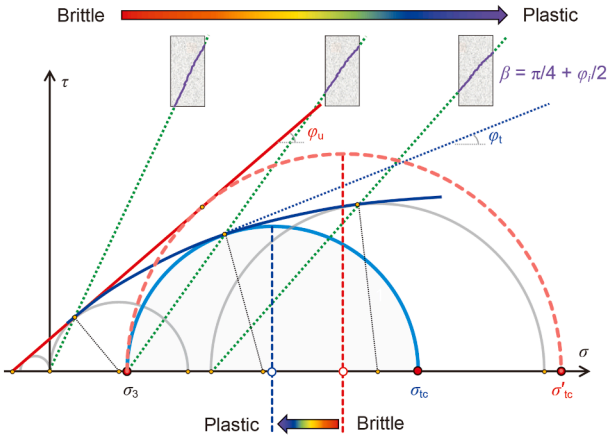

Fig. 23. Variations in the Mohr circle, cohesive strength, and frictional properties across triaxial stress states.

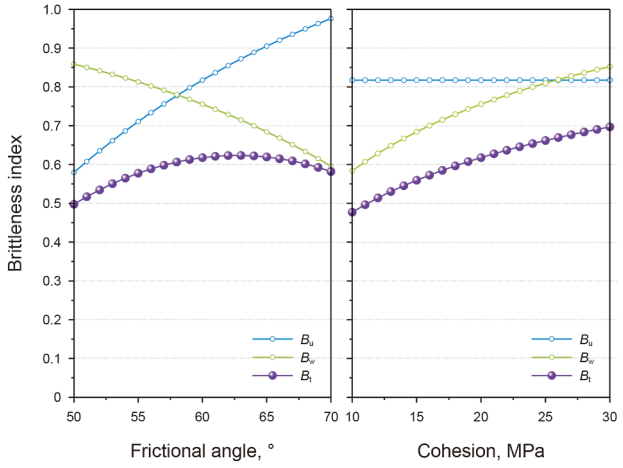

Fig. 24. Variations in the uniaxial brittleness index B_u, weakening coefficient B_w reflecting the effect of confining pressure on brittleness, and triaxial brittleness index B_t with changes in the uniaxial internal friction angle and cohesion.

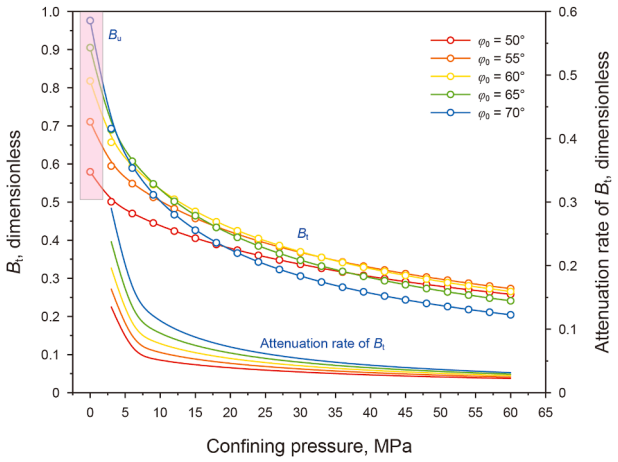

Fig. 25. B_t variation with confining pressure under varying internal friction angles.

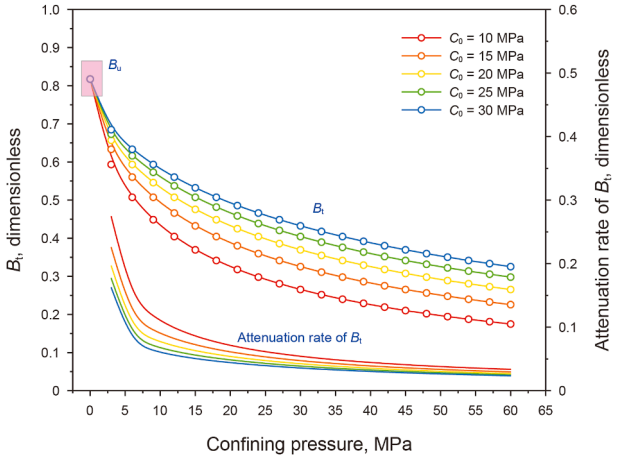

Fig. 26. B_t variation with confining pressure under varying cohesion.

microcrack propagation, leading to energy concentrations that favour tensile-dominated failure. Conversely, under high confining pressures, tensile microcrack formation is significantly limited, and shear microcrack evolution dominates rock failure. In particular, under high internal friction conditions, the energy barrier for shear microcrack generation increases, resulting in reduced rock brittleness. Compared with the internal friction angle, the effect of cohesion on brittleness differs. B_u remains constant as cohesion increases, whereas both B_w and B_t are positively correlated with cohesion. This suggests that under uniaxial stress, cohesion does not affect rock brittleness. However, under confining pressure, increased cohesion enhances the resistance to tensile and shear microcrack formation. Compared with tensile microcracks, shear microcracks require more strain energy to initiate, making them more difficult to extend. Therefore, increased resistance to shear microcrack formation indirectly promotes tensile microcrack development, strengthening the rock's brittleness.

The variations in B_t with confining pressure for different internal friction angles and cohesion values are shown in Figs. 25 and 26, respectively. First, regardless of whether the cohesion or internal friction angle changes, B_t progressively decreases as the confining pressure increases. This trend aligns with typical experimental results from rock triaxial tests. The magnitude of uniaxial brittleness is enhanced by a higher internal friction angle; concurrently, this parameter also decelerates the reduction in triaxial brittleness observed under increasing confining pressure. Specifically, rocks with a higher internal friction angle exhibit greater uniaxial brittleness; however, the extent of the decrease in brittleness under triaxial conditions also intensifies proportionally with confining pressure. In Fig. 26, since uniaxial brittleness is independent of cohesion, the triaxial brittleness index decreases gradually from 0.82 with increasing confining pressure. Furthermore, higher cohesion leads to a diminished decline in triaxial brittleness as the confining pressure increases. This finding indicates that cohesion mitigates the weakening effect of confining pressure on brittleness in triaxial tests.

6. Analysis of shale brittleness anisotropy through CWFS-based brittleness indices

Following the establishment of reliable brittleness indices in this study, the anisotropy of shale brittleness within the Qingshankou Formation was evaluated using the test data presented in Section 3 (see Table 1). The brittleness indices derived by B_u and the resulting failure modes for uniaxially stressed shale samples at different bedding angles (θ) are shown in Fig. 27. The brittleness index decreases progressively with increasing θ over the range of 0°–60°. Similarly, the fracture mechanism changes: at low θ, fractures exhibit a tensile-shear composite nature, whereas at higher θ (e.g., 60°), failure occurs primarily through shear along the bedding planes. At $\theta = 60°$, the brittleness reaches its minimum value. At this angle, the samples develop single planar shear fractures, exhibiting the weakest brittle characteristics. When θ exceeds 60°, the brittleness index increasing again. During this phase, the failure pattern shifts from single-plane shear fracture to multiple longitudinal splitting and tensile fractures, accompanied by a gradual strengthening of the brittle fracture characteristics.

As shown in Fig. 28, the brittleness of shale across different bedding dip angles progressively decreases with increasing confining pressure. When calculated as the standard deviation of the brittleness values, the anisotropy coefficient is maximized under unconfined conditions (uniaxial stress), highlighting that the influence of bedding orientation on brittleness is most pronounced without confining pressure. Moreover, the anisotropy coefficient decreases with increasing confining pressure, which is correlated with a reduction in the brittleness anisotropy exhibited by shale samples with different θ orientations.

The variations in B_t and B_w with θ under different confining pressures, respectively are shown in Figs. 29 and 30. The influence of θ on shale brittleness displays a consistent trend across varying confining pressures: the brittleness initially increases with θ, peaks at an intermediate angle, and subsequently decreases, reaching its lowest value at $\theta = 60°$. Concurrently, higher confining pressures progressively diminish the angular variations in brittleness (B_t). Notably, the orientation (θ) associated with peak brittleness shifts depending on the confining pressure. At atmospheric pressure (uniaxial stress), maximum brittleness occurs when $\theta = 0°$. In contrast, under confining pressures of 10–30 MPa, shale samples oriented at $\theta = 90°$ exhibit the greatest brittleness. The weakening effect of the confining pressure on the brittleness is quantified in Fig. 30 using B_w, where smaller B_w values denote a more pronounced weakening. An examination of the data in Figs. 29 and 30 reveals that shale with $\theta = 0°$ has the highest inherent brittleness, manifested predominantly through a dual-mechanism fracture involving matrix tensile failure and shear slippage along the bedding planes. Under confining pressure, the interfacial tension between mineral particles and shear along the bedding weakness planes are substantially constrained. This culminates in a more pronounced weakening effect of confinement on brittleness. Despite the weaker uniaxial brittleness in vertically

Table 1
Data from tensile and triaxial compressive tests of shale with different θ, along with brittleness evaluation results obtained using the method proposed in this paper.

Dip angle of bedding planes θ, °	Confining pressure σ_3, MPa	Elastic modulus E, GPa	Poisson's ratio	Compressive strength, MPa	Uniaxial brittleness index B_u	Influence coefficient of confining pressure B_w	Triaxial brittleness index B_t
0	0	7.23	0.17	77.33	0.97	/	/
	10	8.98	0.18	128.18	/	0.34	0.33
	20	10.15	0.19	171.33		0.26	0.25
	30	10.31	0.21	199.01		0.21	0.20
15	0	6.98	0.18	60.77	0.92	/	/
	10	7.11	0.20	109.30	/	0.40	0.36
	20	8.54	0.18	118.50		0.24	0.22
	30	9.63	0.22	161.14		0.23	0.21
30	0	6.92	0.11	29.82	0.76	/	/
	10	7.85	0.19	57.50	/	0.40	0.30
	20	9.02	0.20	71.82		0.28	0.21
	30	12.36	0.20	84.50		0.22	0.17
45	0	6.63	0.13	14.40	0.40	/	/
	10	7.56	0.15	30.09	/	0.42	0.17
	20	9.12	0.19	45.81		0.35	0.14
	30	11.19	0.22	77.40		0.42	0.13
60	0	10.58	0.13	10.56	0.29	/	/
	10	10.56	0.17	31.47	/	0.52	0.15
	20	12.88	0.21	43.60		0.39	0.11
	30	13.50	0.19	54.75		0.34	0.10
75	0	12.12	0.17	16.76	0.37	/	/
	10	13.56	0.18	45.20	/	0.63	0.23
	20	14.35	0.20	71.38		0.56	0.21
	30	18.56	0.21	81.97		0.45	0.17
90	0	17.86	0.19	41.04	0.68	/	/
	10	18.85	0.16	86.35	/	0.65	0.45
	20	19.54	0.19	122.30		0.53	0.36
	30	22.35	0.22	146.32		0.45	0.31

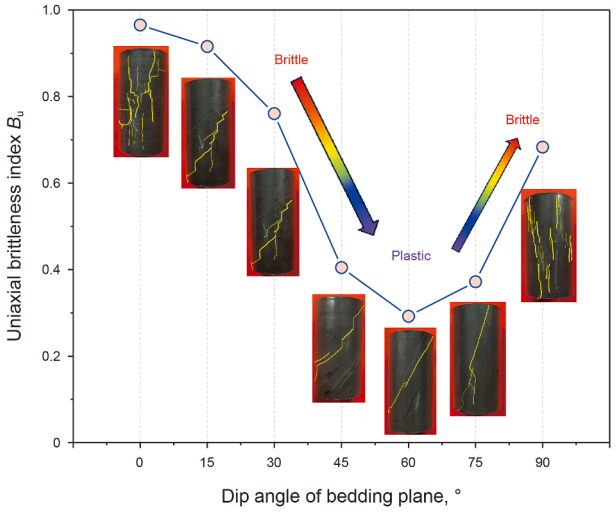

Fig. 27. Changes in the uniaxial brittleness of shale and its corresponding failure mode with variations in θ.

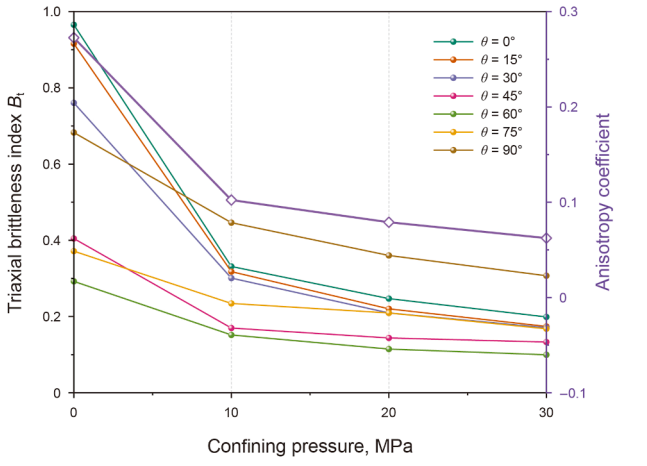

Fig. 28. Variation in the triaxial brittleness indices of shale samples with different θ with confining pressure.

bedded shale (90° dip), the substantially lower resistance to tensile opening along the bedding planes than to matrix tension and bedding shear resistance dictates the failure mode. Under confining pressure, this leads to persistent tensile failure along the bedding, thereby limiting the suppression of brittleness observed at this orientation.

7. Discussion

For unconventional resource engineering (e.g., tight oil, shale oil, and coalbed methane), brittleness is a core determinant. It underpins key applications such as sweet spot prediction, wellbore stability evaluation, and hydraulic fracturing design. As noted previously, diverse fields have developed five distinct brittleness indices, each of which are founded on unique principles and methodologies for characterizing rock failure. However, the broad applicability and reliability of these indices remain contentious. Table 2 summarizes the five key index types and their calculation assumptions. These five typical brittleness indices have been widely used in previous studies, covering key behaviours from macroscopic mineral composition to microscopic energy evolution, and can be used to comprehensively analyse rock brittleness. To compare the anisotropic brittleness of shale, this study utilizes representative indices from these categories alongside the newly developed B_u and B_t. The θ-dependent variations in the

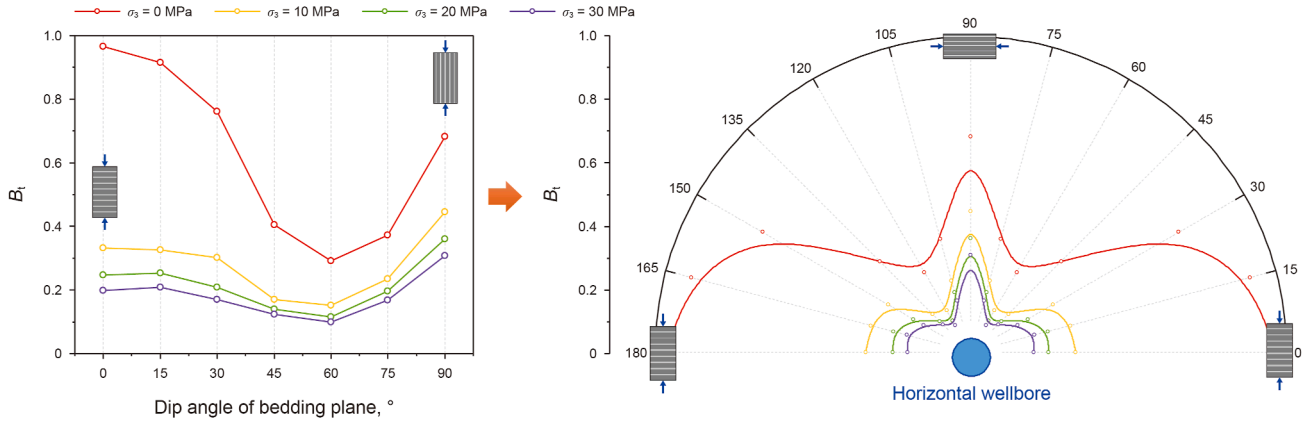

Fig. 29. Dependence of the shale brittleness index (B_t) on θ across variable confining pressures.

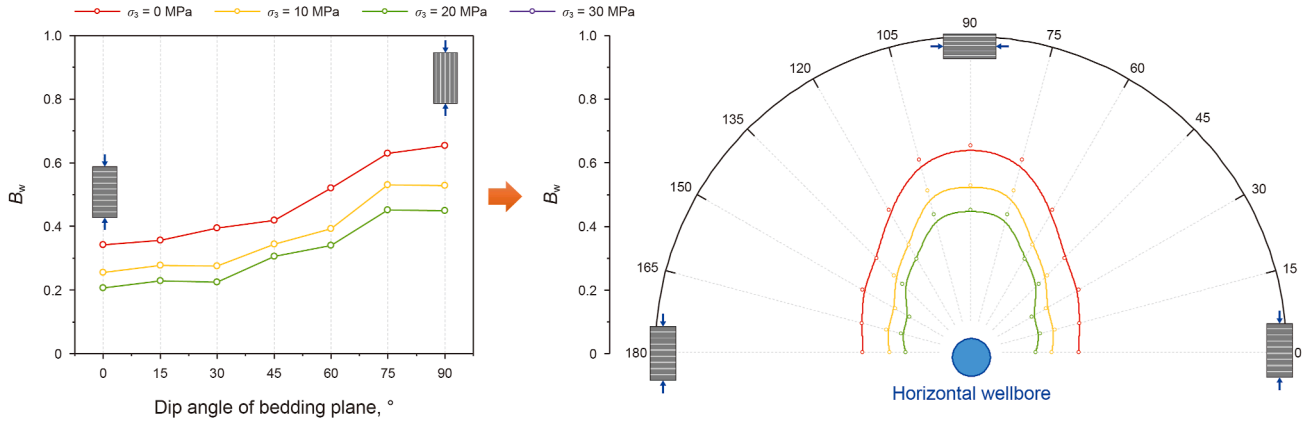

Fig. 30. Dependence of the shale brittleness index (B_w) on θ across variable confining pressures.

Table 2
Brittleness indices of different categories.

Category	Formula	Symbol illustration	Calculability assumption	Reference
Brittleness indices based on mineral content	$B_{mineral} = \frac{W_{qtz} + W_F + W_M + W_{carb}}{W_{tot}}$	W_{tot} is the total amount of rock minerals; W_{qtz}, W_{carb}, W_F, and W_M are the mineral contents of quartz, carbonate, feldspar, and mica, respectively.	Assumes brittle minerals (quartz, feldspar, carbonates) dominate fracture development; ignores mineral grain orientation and distribution; no direct stress-strain relation.	Jin et al. (2014)
Brittleness indices based on elastic parameters obtained from logging data	$B_{elastic} = 0.5(E' + \nu')$	E' and ν' are the normalized elastic modulus and Poisson's ratio, respectively.	Assumes higher E and lower ν imply higher brittleness; derived from well logs without lab calibration; ignores post-peak behaviour and structural anisotropy.	Rickman et al. (2008)
Brittleness indices based on strain parameters	$B_{strain} = \varepsilon_e/\varepsilon_p$	ε_e and ε_p are the reversible strain and total strain at failure, respectively.	Assumes clearly distinguishable elastic and plastic stages; requires full stress-strain curves; sensitive to noise in brittle-ductile transition region.	Hucka and Das (1974)
Brittleness indices based on strength parameters	$B_{strength} = (\tau_p - \tau_r)/\tau_p$	τ_p and τ_r are the peak intensity and residual intensity, respectively.	Assumes strength drop after peak is a valid proxy for brittleness; applicable when residual strength can be accurately identified; hard to apply to ductile specimens.	Bishop (1967)
Brittleness indices based on strain energy	$B_{energy} = \frac{U_f + U_d}{U_{ce} + U_d}$ or $\frac{U_a}{U_{ce} + U_d}$	U_e is the elastic strain energy; U_d is dissipated energy; U_f is the post peak fracture energy; U_a additional energy; U_{ce} is the elastic strain energy consumed.	Assumes complete energy decomposition is possible; requires high-resolution stress–strain data and stable loading system; difficult under complex loading or brittle failure with AE bursts.	Ai et al. (2016)

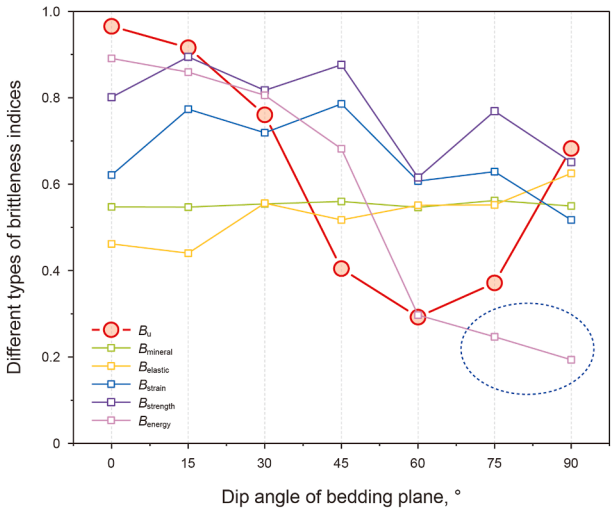

Fig. 31. Evaluation of shale anisotropic brittleness under uniaxial stress using different brittleness indices.

brittleness index evaluations under uniaxial stress are shown in Fig. 31. Shale failure analysis reveals a distinct trend: brittleness reaches a minimum at $\theta = 60°$ (Fig. 27), characterized by predominant shear fracturing, then increases following an initial decline with increasing θ. The evaluation outcomes of B_u reliably characterize this change, underscoring its utility for gauging anisotropic brittleness in shale. The $B_{mineral}$ brittleness index, which is based on the brittle mineral content, is the current standard in oilfield exploration. This preference is driven by the method's operational simplicity and its effective synergy with logging data. However, owing to the inability of mineral content to reflect the influence of shale sedimentary structure, $B_{mineral}$ in Fig. 30 shows almost no change with increasing θ. This is why many rock mechanics scholars and engineers do not recognize this method (Kuang et al., 2021; Zhang et al., 2022; Lei et al., 2023; Alsultan et al., 2023; Yao et al., 2024). $B_{elastic}$, derived from the elastic modulus and Poisson's ratio, exhibits minor fluctuations (typically 0.4–0.6) across θ angles. This limited variation obscures how the brittle fracture behaviour of shale evolves with θ. The main reason is that Poisson's ratio has no significant regularity with θ. B_{strain} and $B_{strength}$ are the brittle indices based on strain parameters and strength parameters, respectively. The consistency between the evaluation results of these two indices and the shale failure patterns in Fig. 25 is also not good. Shale exhibits pronounced brittle behaviour under uniaxial stress, characterized by negligible plastic deformation prior to the peak of the stress-strain curve. Beyond this point, the curve decreases almost linearly, complicating the precise identification of both the yield stress and residual strength. As θ increases from 0° to 60°, the strain-energy-based brittleness index B_{energy} aligns closely with the B_u evaluation and consistently reflects the observed shale fracture progression. However, when θ is 75° and 90°, the change in B_{energy} is opposite that of B_u. For shale samples with bedding planes oriented at 75° and 90° (Fig. 5), failure is dominated by tensile fracturing parallel to the bedding. This process is characterized by significant prepeak oscillations in the measured stress-strain response. Under these conditions, accurate identification of various strain energies becomes very difficult, which also restricts the accurate evaluation of brittleness indices based on strain energy.

The triaxial brittleness of the shale samples with θ of 0° and 90° was evaluated using the different categories of brittleness indices, as shown in Figs. 32 and 33. The inverse relationship between rock brittleness and confining pressure serves as a benchmark in this work for assessing the validity of multiple brittleness indices. The absence of correlation between $B_{mineral}$ and confining pressure in Fig. 29 demonstrates that brittleness indices derived solely from mineral composition cannot incorporate the influence of shale bedding structure on mechanical anisotropy. Consequently, they are inadequate for describing alterations in shale brittleness induced by external stress. The evaluation results of $B_{elastic}$ are positively correlated with the confining pressure, which contradicts objective laws. The primary factor is the positive dependence of $B_{elastic}$'s key parameter, the elastic modulus, on the confining pressure. Consistent with the widely accepted trend of decreasing shale brittleness under elevated confining pressures, the assessments derived from B_{energy} and B_t confirm this relationship. Conversely, B_{strain} and $B_{strength}$ yield nonmonotonic responses. When the confining pressure is increased from 0 to 10 MPa, their values initially increase. However, a subsequent decline emerges as the pressure further increases from 10 to 30 MPa. This pattern for B_{strain} and $B_{strength}$, mirrors that shown in Fig. 33 and aligns

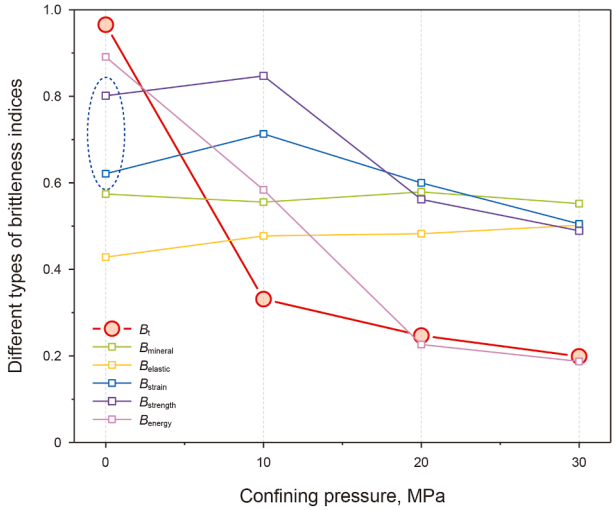

Fig. 32. Evaluation of brittleness of shale under triaxial stress using different categories of brittleness indices ($\theta = 0°$).

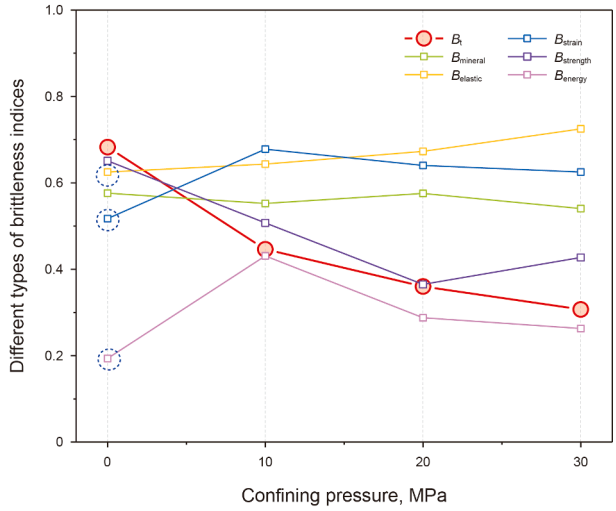

Fig. 33. Evaluation of brittleness of shale under triaxial stress using different categories of brittleness indices ($\theta = 90°$).

with the observations in Fig. 32. Under substantial confining pressures or in rocks with constrained brittleness, the stress-strain profile distinctly manifests a plastic yield phase and a postpeak softening segment. Precise determination of the yield strength and residual strength is crucial for reliable evaluations using these methods. Unfortunately, the reliability of B_{strain} and $B_{strength}$ decreases for highly brittle rocks subjected to low confining pressures. Additionally, the B_{energy} evaluation at a confining pressure of 0 MPa in Fig. 33 proves suboptimal. This stems from significant prepeak fluctuations in the stress-strain curve of the shale under uniaxial loading ($\theta = 90^{\circ}$), complicating the accurate quantification of dissipated energy.

(1) The advantages of the new brittleness index

Shale brittleness arises from the interplay between inherent geological characteristics and external environmental conditions. Primary internal geological influences include brittle mineral content, organic matter abundance, natural fracture networks, bedding planes, and porosity, which collectively govern the compositional and structural mechanical properties of rock. External factors, predominantly burial depth and horizontal stress differentials, modulate shale brittleness through their influence on ambient temperature, confining pressure, and the prevailing stress regime. As a multifaceted mechanical property of rock, brittleness necessitates that any scientifically robust and reliable index captures its intrinsic as well as external characteristics. It needs to not only reflect the differences in intrinsic brittle properties caused by rock lithology but also account for the influence of external conditions on its brittleness. The novel brittleness index introduced in this work effectively captures the dual nature of rock brittleness. Specifically, the uniaxial index (B_u) characterizes the inherent brittleness of rock, independent of external forces. Conversely, the triaxial index (B_t) represents the apparent brittleness manifested under applied stress. This inherent brittleness describes the rock's innate tendency for brittle fracture, which is unaffected by external conditions. Indices derived from mineralogical composition correspond to this inherent type. The apparent brittleness describes how environmental factors modify the inherent brittleness of rocks. While most established brittleness indices capture this phenomenon, they fundamentally neglect the intrinsic role that confining pressure plays in defining brittleness. Rather, they infer the impact of confining pressure indirectly, by leveraging its effect on mechanical parameters. Once the mechanical parameters used in such indices have different effects on brittleness under uniaxial and triaxial stresses, their results will no longer be applicable. For example, under uniaxial stress, the high elasticity of rock materials is considered a significant brittle characteristic, which leads to a positive correlation between $B_{elastic}$ and rock brittleness. However, as the elastic modulus increases with confining pressure, an inverse relationship is observed between $B_{elastic}$ and rock brittleness under triaxial stress conditions (Figs. 32 and 33). To overcome this limitation, the present study introduces a novel triaxial brittleness index. This index is derived from the multiplicative combination of the uniaxial brittleness index (representing inherent brittleness) and a coefficient that quantifies the diminishing effect of confining pressure on brittleness. Consequently, the proposed index demonstrates improved predictive capacity for both differentiating brittleness variations across rock types and quantitatively evaluating the evolution of reservoir rock brittleness under varying external stresses.

(2) Operability and scalability of the brittleness index in this article

Unlike construction and mining engineering, oil and gas engineering is typically carried out at depths of several kilometre underground. There are usually dozens of shale formations with different lithologies in the vertical direction. Therefore, underground rock cores suitable for mechanical experiments are extremely scarce and valuable. It is unrealistic to conduct brittleness evaluations through indoor mechanical experiments for all strata at different depths. Therefore, oil and gas exploration and development require a brittleness evaluation index to be effectively combined with geophysical logging curves to achieve rapid, continuous, and economical evaluation of reservoir brittleness profiles. Although the brittleness index based on brittle minerals has limitations on a scientific basis, it has become the most widely used method because of its ease of calculation through logging curves. In contrast, although the strain energy brittleness index has a sufficient physical basis, its key parameters (such as dissipated energy) are difficult to obtain stably and reliably directly from conventional logging data, making it difficult to widely apply in the field of petroleum and natural gas engineering.

The brittleness index established in this article not only has advantages in terms of scientific principles but also has advantages in terms of operability and scalability. The operability of combining it with logging data is reflected mainly in the following aspects: the acquisition of index core parameters (cohesion, internal friction angle, and compressive strength) does not rely on complex specialized logging projects but can rely on existing mature logging interpretation theories and models to complete predictions and calculations through conventional logging data (such as the acoustic time difference, i.e., Eq. (15), Radwan and Sen, 2021), which can adapt to the conventional logging data processing system at oil and gas exploration sites and reduce the technical threshold and operating costs in practical applications. Moreover, the combination of the brittleness index and logging data has a good applicability: on the one hand, its parameter prediction model can be adaptively adjusted on the basis of the geological characteristics of shale in different regions and rock types. By matching a small amount of indoor mechanical experimental data with logging data, the index can be applied to new exploration blocks to avoid applicability limitations caused by differences in geological conditions. On the other hand, the index calculation results can be linked with other logging interpretation results (such as lithology identification, porosity evaluation, geostress prediction, etc.) and integrated into the "lithology-physical property-brittleness sweet spot" integrated evaluation process of shale reservoirs. This not only enables the construction of continuous brittleness profiles for the entire well section of a single well but also further supports the lateral comparison and planar distribution analysis of brittleness between multiple wells, providing a more systematic logging interpretation basis for engineering decisions such as optimizing horizontal well trajectories and optimizing fracturing intervals in shale gas development. This combination of scalability and operability not only solves the practical problem of indoor experiments being difficult to cover the entire well section but also meets the multiscale needs of oil and gas exploration and development from single-well evaluation to regional research, further highlighting the application value of the brittleness index in engineering practice.

$$\begin{cases} \varphi = \sin^{-1}\left(\dfrac{V_p - 1}{V_p + 1}\right) \\ C = \dfrac{UCS\cos\varphi}{2(1 - \sin\varphi)} \end{cases} \tag{15}$$

(3) Future research directions

The CWFS model simulates the failure process of rocks through cohesive degradation and friction strengthening, successfully capturing the key transition mechanism of brittle rocks from peak strength to residual strength, and providing a clear framework for the physical basis of the brittleness index in this study. However, there is still much room for improvement in the brittleness index established in this article. For example, in the process of oilfield development, owing to changes in pore pressure, underground stress also undergoes dynamic evolution. However, the static brittleness index established in this article cannot currently describe this process. To more accurately determine the dynamic evolution of cohesion and friction angle under complex stress states such as high constraint pressure, future research can combine microscopic experimental techniques, such as scanning electron microscopy (SEM) and X-ray tomography (CT), to observe the microstructural changes in heterogeneous rocks during loading, obtain more detailed information on the evolution of cohesion and friction angle, and optimize and improve the CWFS model. Moreover, numerical simulation methods such as the discrete element method (DEM) and finite element method (FEM) can be used to simulate the failure process of heterogeneous rocks under different stress conditions, improve the brittleness evaluation method in this paper, and provide theoretical support for improving the accuracy of the brittleness index evaluation.

8. Conclusions

Understanding the anisotropic behaviour of shale brittleness is critically important for optimizing drilling and hydraulic fracturing design in shale resource development. Given that conventional brittleness indices inadequately account for the anisotropy and confining pressure dependence of shale, a series of triaxial mechanical tests were conducted on the Qingshankou Formation shale in this study. On the basis of key mechanical parameters derived from these tests and the use of the CWFS model, a novel triaxial brittleness assessment metric was developed to characterize shale brittleness anisotropy. The results demonstrate the following:

(1) Under uniaxial stress, shale failure modes evolve with increasing θ, progressing from composite matrix tension-bedding shear fractures, through a dominant bedding shear fracture, to multiple bedding tensile splitting fractures. Concurrently, shale brittleness initially decreases but then increases as θ increases. Under confining pressure (triaxial stress), the brittle characteristics of shale are generally suppressed across all θ angles; however, the fundamental pattern of brittle fracture evolution remains consistent regardless of θ.
(2) For shale under uniaxial loading and triaxial loading, the compressive strength, cohesion, and internal friction angle exhibit a consistent trend: the values initially decrease before increasing as the bedding angle θ increases. Higher confining pressures progressively reduce the anisotropy of these mechanical parameters. Meanwhile, the elastic modulus under varying confining pressures progressively increases, followed by accelerated growth with increasing θ angle. In contrast, the Poisson's ratio remains largely unaffected by θ across all confining pressures.
(3) Rock fracture response fundamentally arises from the interplay between cohesive strength and frictional resistance. Within the CWFS framework, the mobilization of these components corresponds to distinct energy pathways: cohesive strength is linked to elastic energy accumulation and release, while frictional resistance governs dissipative energy processes. This coupled mobilization constitutes the primary mechanism driving rock brittle fracture.
(4) Capitalizing on the established link between cohesive/frictional mobilization dynamics and brittle fracture, a novel triaxial brittleness index was developed. This index integrates a uniaxial component capturing the material's inherent brittleness and a degradation coefficient quantifying the suppression of brittleness under confining stress. Critically, this approach not only characterizes the directional brittleness of shale across various bedding plane orientations (θ) under uniaxial conditions but also quantitatively tracks how this anisotropic brittleness evolves with increasing confinement.
(5) Under uniaxial stress, shale brittleness anisotropy is most pronounced and displays a unimodal variation with θ. The maximum brittleness occurs at $\theta = 0^\circ$, whereas the minimum is observed at $\theta = 60^\circ$. Elevated confining pressure alters this anisotropy in two key ways. First, the brittleness anisotropy coefficient decreases progressively as the confining pressure increases. Second, the orientation of the peak brittleness shifts to $\theta = 90^\circ$. This demonstrates that confining pressure degrades shale brittleness differently depending on θ, with the most substantial degradation effect occurring at $\theta = 0^\circ$.
(6) The brittleness index developed in this study advances upon existing models by integrating both inherent and apparent brittleness components, resulting in a more physically comprehensive measure. Compared with established indices, it demonstrates heightened sensitivity to lithological properties and external stress states. Furthermore, its compatibility with geophysical data enhances its potential for practical application. This reliable model provides significant utility for guiding sweet spot identification, wellbore stability assessment, and fracturing optimization in shale oil and gas exploration and development.
(7) In this study, a static brittleness index is established, which cannot characterize the brittle evolution process that occurs during oilfield development because of the dynamic evolution of in-situ stress. This is our future research direction. In the future, we will combine micro experimental techniques and discrete element numerical methods to explore the failure process of heterogeneous rocks under different stress conditions, especially under dynamic stress, to improve our brittleness evaluation method.

CRediT authorship contribution statement

Jun Zhang: Writing – original draft, Investigation. **Jin-Yuan Zhang:** Writing – original draft, Methodology. **Jia Zeng:** Writing – review & editing, Software. **Zhe-Jun Pan:** Writing – review & editing. **Yu-Wei Li:** Writing – review & editing. **Zi-Yuan Cong:** Writing – review & editing.

Declaration of competing interest

The authors declare that they have no known competing financial interests or personal relationships that could have appeared to influence the work reported in this paper.

Acknowledgement

The research was supported by the National Natural Science Foundation of China Joint Fund Project (Grant No. U24B6004), the China Postdoctoral Science Foundation (Grant No. 2024MD763934), the Postdoctoral Science Foundation of Heilongjiang Province (Grant No. LBH-Z24106).

References

Ai, C., Zhang, J., Li, Y.W., et al., 2016. Estimation criteria for rock brittleness based on energy analysis during the rupturing process. Rock Mech. Rock Eng. 49, 4681–4698. https://doi.org/10.1007/s00603-016-1078-x.

Akdag, S., Karakus, M., Nguyen, G.D., et al., 2021. Evaluation of the propensity of strain burst in brittle granite based on post-peak energy analysis. Undergr. Space 6 (1), 1–11. https://doi.org/10.1016/j.undsp.2019.08.002.

Allaby, A., Allaby, M., 1990. The Concise Oxford Dictionary of Earth Sciences. OUP. https://api.semanticscholar.org/CorpusID:128862482.

Altindag, R., 2003. Correlation of specific energy with rock brittleness concepts on rock cutting. J. South. Afr. Inst. Min. Metall. 103 (3), 163–171. https://hdl.handle.net/10520/AJA0038223X_2948.

Altindag, R., 2010. Assessment of some brittleness indexes in rock-drilling efficiency. Rock Mech. Rock Eng. 43, 361–370. https://doi.org/10.1007/s00603-009-0057-x.

Alzahabi, A., AlQahtani, G., Soliman, M.Y., et al., 2015. Fracturability index is a mineralogical index: A new approach for fracturing decision. In: SPE Saudi Arabia Section Annual Technical Symposium and Exhibition. https://doi.org/10.2118/178033-MS.

Andreev, G.E., 1995. Brittle Failure of Rock Materials: Test Results and Constitutive Models. CRC press. https://api.semanticscholar.org/CorpusID:127541458.

Alsultan, Q.H., Panessai, I.Y., Abed, T., et al., 2023. Innovative composite materials for improving structural integrity and longevity in civil engineering applications. Khwarizmia 63–72. https://doi.org/10.70470/KHWARIZMIA/2023/006.

Barton, N., 1976. The shear strength of rock and rock joints. Int. J. Rock Mech. Min. Sci. Geomech. Abstr. 13 (9), 255–279. https://doi.org/10.1016/0148-9062(76)90003-6.

Bishop, A.W., 1967. Progressive failure with special reference to the mechanism causing it. Proc Geotech Conf, Oslo. 2, 142–150. https://cir.nii.ac.jp/crid/1573387449645087744.

Byerlee, J.D., 1968. Brittle-ductile transition in rocks. J. Geophys. Res. 73 (14), 4741–4750. https://doi.org/10.1029/JB073i014p04741.

Cheng, H., Yang, X., Yang, D., et al., 2024. Evaluation method of rock brittleness based on post-peak energy conversion under monotonic and cyclic triaxial compression. Bull. Eng. Geol. Environ. 83 (7), 279. https://doi.org/10.1007/s10064-024-03728-4.

Dong, Q., Kang, J., Sun, J., et al., 2024. Experimental study on anisotropic mechanical characteristics of shale under triaxial loading. Appl. Sci. 14 (9), 3849. https://doi.org/10.3390/app14093849.

Geng, Z., Chen, M., Jin, Y., et al., 2016. Experimental study of brittleness anisotropy of shale in triaxial compression. J. Nat. Gas Sci. Eng. 36, 510–518. https://doi.org/10.1016/j.jngse.2016.10.059.

Glorioso, J.C., Rattia, A., 2012. Unconventional reservoirs: Basic petrophysical concepts for shale gas. In: SPE/EAGE European Unconventional Resources Conference and Exhibition. https://doi.org/10.2118/153004-MS.

Gong, X., Sun, C.C., 2015. A new tablet brittleness index. Eur. J. Pharm. Biopharm. 93, 260–266. https://doi.org/10.1016/j.ejpb.2015.04.007.

Gu, M., Sheng, M., Ren, L., et al., 2024. Synchronous vertical fracture propagation of multi-layer radial wells for enhancing stimulated height in shale oil reservoir. J. Rock Mech. Geotech. Eng. 17 (9), 5542–5559. https://doi.org/10.1016/j.jrmge.2024.09.026.

Gui, J., Guo, J., Sang, Y., et al., 2023. Evaluation on the anisotropic brittleness index of shale rock using geophysical logging. Petroleum 9 (4), 545–557. https://doi.org/10.1016/j.petlm.2022.06.001.

Gui, J., Ma, T., Chen, P., et al., 2018. Anisotropic damage to hard brittle shale with stress and hydration coupling. Energies 11 (4), 926. https://doi.org/10.3390/en11040926.

Guo, J.C., Zhao, Z.H., He, S.G., et al., 2015. A new method for shale brittleness evaluation. Environ. Earth Sci. 73, 5855–5865. https://doi.org/10.1007/s12665-015-4268-z.

Hajiabdolmajid, V., Kaiser, P., 2003. Brittleness of rock and stability assessment in hard rock tunneling. Tunn. Undergr. Space Technol. 18 (1), 35–48. https://doi.org/10.1016/S0886-7798(02)00100-1.

Heng, S., Guo, Y., Yang, C., et al., 2015. Experimental and theoretical study of the anisotropic properties of shale. Int. J. Rock Mech. Min. Sci. 74, 58–68. https://doi.org/10.1016/j.ijrmms.2015.01.003.

Holt, R.M., Fjær, E., Stenebråten, J.F., et al., 2015. Brittleness of shales: Relevance to borehole collapse and hydraulic fracturing. J. Petrol. Sci. Eng. 131, 200–209. https://doi.org/10.1016/j.petrol.2015.04.006.

Hucka, V., Das, B., 1974. Brittleness determination of rocks by different methods. Int. J. Rock Mech. Min. Sci. Geomech. Abstracts 11 (10), 389–392. https://doi.org/10.1016/0148-9062(74)91109-7.

Jarvie, D.M., Hill, R.J., Ruble, T.E., et al., 2007. Unconventional shale-gas systems: The Mississippian Barnett shale of north-central Texas as one model for thermogenic shale-gas assessment. AAPG Bull. 91 (4), 475–499. https://doi.org/10.1306/12190606068.

Jia, C., Zhang, Q., Lei, M., et al., 2021. Anisotropic properties of shale and its impact on underground structures: An experimental and numerical simulation. Bull. Eng. Geol. Environ. 80 (10), 7731–7745. https://doi.org/10.1007/s10064-021-02428-7.

Jiang, W., Lai, Y., Ma, Q., et al., 2023. Mechanical damage model and brittleness index of frozen rocks based on statistical damage theory. Acta Geotechnica 18 (9), 4687–4713. https://doi.org/10.1007/s11440-023-01861-0.

Jin, X., Shah, S.N., Roegiers, J.C., et al., 2014. Fracability evaluation in shale reservoirs-an integrated petrophysics and geomechanics approach. In: SPE Hydraulic Fracturing Technology Conference. https://doi.org/10.2118/168589-MS.

Kong, L., Xie, H., Gao, C., et al., 2022. Experimental and theoretical research on the anisotropic deformation and energy evolution characteristics of shale under uniaxial cyclic loading and unloading. Int. J. GeoMech. 22 (11), 04022208. https://doi.org/10.1061/(ASCE)GM.1943-5622.0002590.

Kuang, Z., Qiu, S., Li, S., et al., 2021. A new rock brittleness index based on the characteristics of complete stress–strain behaviors. Rock Mech. Rock Eng. 54, 1109–1128. https://doi.org/10.1007/s00603-020-02311-z.

Lei, W., Liu, X., Ding, Y., et al., 2023. The investigation on shale mechanical characteristics and brittleness evaluation. Sci. Rep. 13 (1), 22936. https://doi.org/10.1038/s41598-023-49934-0.

Li, Y., Jia, D., Rui, Z., et al., 2017. Evaluation method of rock brittleness based on statistical constitutive relations for rock damage. J. Petrol. Sci. Eng. 153, 123–132. https://doi.org/10.1016/j.petrol.2017.03.041.

Liang, L., Liu, X., Xiong, J., et al., 2017. New model to evaluate the brittleness in shale formation. In: International Geophysical Conference, pp. 1248–1251. https://doi.org/10.1190/IGC2017-317.

Liu, Y., Li, Z., Zhao, S., et al., 2024. Effects of inclination angle and confining pressure on triaxial unloading-induced slip behaviors of shale fractures. Front. Earth Sci. 12, 1372839. https://doi.org/10.3389/feart.2024.1372839.

Ma, T., Liu, K., Su, X., et al., 2024. Investigation on the anisotropy of mesomechanical properties of shale rock using micro-indentation. Bull. Eng. Geol. Environ. 83 (1), 29. https://doi.org/10.1007/s10064-023-03510-y.

Ma, T., Wang, H., Liu, Y., et al., 2023. Experimental investigation on the anisotropy of mode-I fracture and tensile failure of layered shale. Eng. Fract. Mech. 290, 109484. https://doi.org/10.1016/j.engfracmech.2023.109484.

Özfirat, M.K., Yenice, H., Şimşir, F., et al., 2016. A new approach to rock brittleness and its usability at prediction of drillability. J. Afr. Earth. 119, 94–101. https://doi.org/10.1016/j.jafrearsci.2016.03.017.

Patel, R., Zhang, Y., Lin, C.W., et al., 2022. Microstructural and mechanical property characterization of Argillaceous, Kerogen-rich, and Bituminous shale rocks. J. Nat. Gas Sci. Eng. 108, 104827. https://doi.org/10.1016/j.jngse.2022.104827.

Radwan, A., Sen, S., 2021. Stress path analysis for characterization of *in situ* stress state and effect of reservoir depletion on present-day stress magnitudes: Reservoir geomechanical modeling in the Gulf of Suez Rift Basin, Egypt. Nat. Resour. Res. 30 (1), 463–478. https://doi.org/10.1007/s11053-020-09731-2.

Ramsay, J.G., 1967. Folding and Fracturing of Rocks. McGraw-Hill, 568. https://books.google.com/books?id=IicUAQAAIAAJ.

Rickman, R., Mullen, M., Petre, E., et al., 2008. A practical use of shale petrophysics for stimulation design optimization: all shale plays are not clones of the Barnett shale. In: SPE Annual Technical Conference and Exhibition. https://doi.org/10.2118/115258-MS.

Sari, M., 2018. Investigating relationships between engineering properties of various rock types. GJESE 5 (1), 1–25. https://doi.org/10.15377/2409-5710.2018.05.1.

Shen, B., Shi, J., Barton, N., 2018. An approximate nonlinear modified Mohr-Coulomb shear strength criterion with critical state for intact rocks. JRMGE 10 (4), 645–652. https://doi.org/10.1016/j.jrmge.2018.04.002.

Tarasov, B.G., Randolph, M.F., 2011. Superbrittleness of rocks and earthquake activity. Int. J. Rock Mech. Min. Sci. 48 (6), 888–898. https://doi.org/10.1016/j.ijrmms.2011.06.013.

Ulusay, R., 2015. The ISRM Suggested Methods for Rock Characterization, Testing and Monitoring: 2007–2014. Springer International Publishing, Cham, Switzerland. https://doi.org/10.1007/978-3-319-07713-0.

Wang, C., Li, S., Zhang, D., et al., 2023. Study on the effects of water content and layer orientation on mechanical properties and failure mechanism of shale. Energy 271, 127050. https://doi.org/10.1016/j.energy.2023.127050.

Wang, F.P., Gale, J.F., 2009. Screening criteria for shale-gas systems. Transactions-GCAGS 59, 779–794. https://www.tib.eu/de/suchen/id/BLSE%3ARN271832836.

Wang, H., Liu, D.A., Huang, Z., et al., 2017a. Mechanical properties and brittleness evaluation of layered shale rock. Eng. Geol. 25 (6), 1414–1423. http://en.dzkx.org/article/doi/10.13544/j.cnki.jeg.2017.06.003.

Wang, Y., Li, C.H., 2017. Investigation of the P-and S-wave velocity anisotropy of a Longmaxi formation shale by real-time ultrasonic and mechanical experiments under uniaxial deformation. J. Petrol. Sci. Eng. 158, 253–267. https://doi.org/10.1016/j.petrol.2017.08.054.

Wang, Y., Li, C.H., Hu, Y.Z., et al., 2017b. A new method to evaluate the brittleness for brittle rock using crack initiation stress level from uniaxial stress–strain curves. Environ. Earth Sci. 76, 1–18. https://doi.org/10.1007/s12665-017-7117-4.

Wu, Y., Li, Y., Luo, S., et al., 2020. Multiscale elastic anisotropy of a shale characterized by cross-scale big data nanoindentation. Int. J. Rock Mech. Min. Sci. 134, 104458. https://doi.org/10.1016/j.ijrmms.2020.104458.

Xia, Y.J., Li, L.C., Tang, C.A., et al., 2017. A new method to evaluate rock mass brittleness based on stress–strain curves of class I. Rock Mech. Rock Eng. 50, 1123–1139. https://doi.org/10.1007/s00603-017-1174-6.

Xia, Y., Zhou, H., Zhang, C., et al., 2022. The evaluation of rock brittleness and its application: A review study. Eur. J. Environ. Civ. Eng. 26 (1), 239–279. https://doi.org/10.1080/19648189.2019.1655485.

Yan, Z., Wang, F., Liu, Y., et al., 2025. Effects of CO_2 pressure on the dynamic wettability of the kerogen surface: Insights from a molecular perspective. Appl. Surf. Sci. 694, 162822. https://doi.org/10.1016/j.apsusc.2025.162822.

Yang, S.Q., Yin, P.F., Ranjith, P.G., 2020. Experimental study on mechanical behavior and brittleness characteristics of Longmaxi Formation shale in Changning, Sichuan Basin, China. Rock Mech. Rock Eng. 53, 2461–2483. https://doi.org/10.1007/s00603-020-02057-8.

Yao, T., Qian, L., Mo, Z., et al., 2024. A new brittleness index based on crack characteristic stress and its engineering applications. Eng. Geol. 330, 107411. https://doi.org/10.1016/j.enggeo.2024.107411.

Zhang, D., Ranjith, P.G., Perera, M.S.A., 2016. The brittleness indices used in rock mechanics and their application in shale hydraulic fracturing: A review. J. Petrol. Sci. Eng. 143, 158–170. https://doi.org/10.1016/j.petrol.2016.02.011.

Zhang, J., Ai, C., Li, Y.W., et al., 2017. Brittleness evaluation index based on energy variation in the whole process of rock failure. CJRME 36 (6), 1326–1340. http://www.rockmech.org/EN/10.13722/j.cnki.jrme.2016.0839.

Zhang, J., Xie, Z., Pan, Y., et al., 2023a. Synchronous vertical propagation mechanism of multiple hydraulic fractures in shale oil formations interlayered with thin sandstone. J. Petrol. Sci. Eng. 220, 111229. https://doi.org/10.1016/j.petrol.2022.111229.

Zhang, J., Yu, Q., Li, Y., et al., 2023b. Hydraulic fracture vertical propagation mechanism in interlayered brittle shale formations: An experimental investigation. Rock Mech. Rock Eng. 56 (1), 199–220. https://doi.org/10.1007/s00603-022-03094-1.

Zhang, X., Xu, J., Shaikh, F., et al., 2022. Rock brittleness evaluation index based on ultimate elastic strain energy. Processes 10 (7), 1367. https://doi.org/10.3390/pr10071367.